Journal of Materials Research and Technology 35 (2025) 7253–7272

Contents lists available at ScienceDirect

Journal of Materials Research and Technology

journal homepage: www.elsevier.com/locate/jmrt

Investigation of the mechanisms affecting corrosion susceptibility of wrought aeronautical aluminium alloys Al–Cu–Li (AA2198) and Al–Cu–Mg (AA2024) for different pre-stretching levels

Christina Margarita Charalampidou [a], Christiaan C.E. Pretorius [b], Muhammed Salojee [b], Dionysios Karousos [a], Malika Khodja [b], Roelf J. Mostert [b,*], Nikolaos D. Alexopoulos [a,**]

[a] University of the Aegean, School of Engineering, Department of Financial Engineering, Research Unit of Advanced Materials, 821 32, Chios, Greece
[b] University of Pretoria, Department of Material Sciences and Metallurgical Engineering, 395, Pretoria, Republic of South Africa

ARTICLE INFO

Handling editor: SN Monteiro

Keywords:
A. aluminium alloys
B. SEM
C. exfoliation corrosion
C. hardening
C. fracture
C. hydrogen embrittlement

ABSTRACT

Aluminium (Al) alloy sheets are usually stretched to manufacture aircraft structures with complex geometries. The corrosion susceptibility of AA2198 Al alloy is examined as a function of the extent of pre-stretching, using a wide range of advanced microscopy, electrochemical techniques, and tensile mechanical testing. Intergranular corrosion attack manifested in sub-surface secondary cracking for the 1.5 % pre-stretching level. A mechanism of deformation-induced chemical heterogeneity is believed to be responsible for the resulting intergranular corrosion, in which δ'-phase nucleation following pre-stretching allows for the removal of matrix Li within highly deformed grains, creating a micro-galvanic coupling between neighbouring grains. At pre-stretching levels of 4.0 % and higher, a transition to transgranular corrosion was observed, whilst the electron backscattered diffraction results indicated that recovery occurs at these pre-stretching levels. At 7.5. % pre-stretching level, the charge transfer resistance values were essentially increased due to the segregation of Li to sub-grain boundaries, allowing for more matrix Li removal and, hence, to the more rapid transgranular attack. On the contrary, the level of corrosion degradation of the tensile properties of AA2024-T3, although being more severe than that of the AA2198 alloy, is not essentially influenced by varying the extent of pre-stretching.

1. Introduction

The increasing interest in environmental protection, and more precisely the rigorous requirements of fuel efficiency and greenhouse gas emissions, have triggered the development of lightweight materials in aerospace industry [1-3]. Employing third-generation Al–Cu–Li alloys is an efficient and favoured approach to achieve weight targets, since Li has the lowest density of all metals [4]. Among commercially available third generation Al–Li alloys, the Aluminium Alloy (AA) 2198 is the most advanced, being used as fuselage skin sheet material in the Airbus A350 and as material of fuselage elements and the second stage fuel tanks for the SpaceX Falcon 9 Spacecraft [5]. It was developed to replace the conventional Al–Cu–Mg alloys (*e.g.,* AA2024 and AA2524) in aircraft structures, where damage tolerance is the critical design factor [6]. This is due to improved mechanical properties [7] and corrosion resistance of these alloys when compared to the conventional Al–Cu–Mg alloys [8-10]. According to articles by Moreto et *al.* 11,12, AA2198-T851 presented higher yield stress and ultimate tensile strength values than AA2524-T3 and better long-term corrosion resistance, despite the more negative corrosion potential due to the presence of Li. Significant differences in the mechanisms of corrosion attack between Al–Cu–Li and conventional Al–Cu–Mg alloys were reported by Milagre et *al.* [13] and Araujo et *al.* [14]. Al–Cu–Li alloys were found to be susceptible to intragranular [13], transgranular as well as exfoliation corrosion attack with variations in the level of susceptibility between the different thermomechanical tempers [14], highlighting the effect of micro-constituent particles on the corrosion mechanism; the predominant corrosion mechanism of Al–Cu–Mg 2024-T3 alloy was intergranular corrosion (IGC).

The enhanced mechanical performance and damage tolerance of Al–Cu–Li alloys are ascribed to their complex precipitation hardening system. This includes several intermetallic phases and dispersoids,

* Corresponding author.
** Corresponding author.
E-mail addresses: roelf.mostert@up.ac.za (R.J. Mostert), nalexop@aegean.gr (N.D. Alexopoulos).

https://doi.org/10.1016/j.jmrt.2025.03.084
Received 25 June 2024; Received in revised form 7 March 2025; Accepted 9 March 2025
Available online 11 March 2025

where δ (Al_3Li), T_1 (Al_2CuLi), θ (Al_2Cu) and S (Al_2CuMg) are the main strengthening phases 15,16. Precipitation of such strengthening phases and their interaction with dislocations may influence both the mechanical strength properties and corrosion resistance of 2xxx series Al alloys. The T_1 precipitate is the major strengthening phase of these alloys because it can remain coherent with Al-matrix even after prolonged ageing and subsequent coarsening while it is sheared only by single dislocations at a specific region, thus hindering strain localisation [17]. Nevertheless, it acts as non-shearable obstacle in later stages of ageing (over-ageing) and has to be bypassed by dislocations during deformation [18-22]. These precipitates nucleate heterogeneously on dislocations, sub-grain boundaries and grain boundaries [23-26]. Differences in the electrochemical potential of these phases with either the Al-matrix or other adjacent phases can trigger corrosion attack [26-29]. Signs of intergranular/inter-subgrannular corrosion susceptibility were found in Al–Cu–Li alloys due to preferential precipitation of Li-rich precipitates such as T_1 and/or δ on grain boundaries. The corrosion was found to initiate within grains with high stored energy (dislocation content), where high concentrations of (dislocation assisted) T_1 nucleation occurred and extended along their periphery (grain boundaries) because of chemical heterogeneity regarding surrounding (less deformed/lower T_1 volume fraction) boundaries. Thereafter, corrosion follows along preferred paths, such as grain-boundaries and sub-grain boundaries 30, 31. Formation of such phases is highly dependent on the Cu/Li ratio, minor solute element content as well as the thermomechanical conditions and heat-treatments the alloy has been subjected to during manufacturing 32,33. Commercial wrought Al alloys of 2xxx series were found to have increased corrosion resistance when artificially aged at certain tempers, such as T6 or T8 34,35. Additionally, severe localized corrosion attack associated with micrometric precipitates [36] was revealed at the slip bands of high energy grains, which were introduced by the stretching process on AA2198-T851 alloy [37]. In particular, T8X temper variations of 2198 aluminium alloy, *i.e.,* solution heat treatment, followed by cold working with X % strain hardening and a final artificial ageing, combine high compressive strength and toughness, which renders them as good substitutes for conventional 2024-T3 and 2524-T3/351 alloys in fuselage/pressure cabin skins [38].

Additionally, since conventional metal fabrication techniques, *i.e.*, forming and casting methods, powder metallurgy, welding, as well as production processes of aircraft components, *i.e.*, heat treatments and refining are constantly advancing to reach higher productivity and formability, alloys such as AA2198-T8X which offer more options for heat-treatability (*e.g.,* hot stamping) are also desired for achieving simplifications in the production chain [39]. The conventional manufacturing procedure for Al aerospace plate and/or sheets usually includes a cold working operation following the solution heat treatment. The aim of this step is to relieve residual stresses, developed during quenching, by means of introducing between 2 and 5 % plastic deformation, as well as providing a good distribution of dislocations to act as precipitate nucleation sites [40]. Regarding Al–Cu–Li alloys, the deformation process is crucial for T_1 phase precipitation, since it preferably nucleates on dislocations formed during this step. It is generally accepted, that pre-stretching in conjunction with artificial ageing increases dislocation density within the Al-matrix [41–43], which act as nucleation sites for the precipitation of the strengthening phases, thus leading to improved mechanical performance [44–46]. Pre-stretching of Al–Cu–Li alloy 2195 at high strain levels (close to plastic instability, 15 %) revealed a continuous refinement (decrease in diameter and narrowing of size distribution) of the T_1 precipitates, along with an increase in their number and density. This was attributed to an increase in dislocation density, as well as a more uniform distribution of the dislocations with increasing stretching level and resulted in significant increases of the T8 yield strength. However, the contribution of T_1 precipitates to the improvement of the mechanical strength properties was reduced with increasing pre-stretching levels, with the increase in mechanical strength at high levels of pre-stretching attributed to the high level of strain hardening retained in the material following artificial ageing [47].

For the AA2099 Al–Cu–Li alloy, similar findings were detailed by Huang *et* al. [48], demonstrating that the dislocation distribution within the deformed AA2099 microstructure is significantly dependent on the orientation of the grains. Some grains were shown to have experienced localized plastic deformation, which in turn favoured the nucleation of the highly electrochemically active T_1 precipitates, leading to their selective localized corrosion. They further proved the preferential nucleation of T_1 precipitates on slip bands. The same research group published similar work [49], investigating why only certain grains showed preferential corrosion attack. It was found that grains with high stored energy containing more crystallographic defects, displayed reduced corrosion resistance, partly due to the preferential precipitation of the T_1 phase on the dislocations. Through electron backscattered diffraction (EBSD), they found that localised corrosion was confined to parent grains with subgrains present in the form of low angle grain boundaries. Furthermore, they found that corrosion was more prevalent along grain boundaries as opposed to grain interiors. Grains with higher stored energy were selectively attacked. Similar behaviour has also been noticed for AA2024 [50] where intergranular corrosion was found to be mainly ascribed to the joint effect of grain boundary composition and stored energy distribution. According to Zang *et* al. [51], intergranular corrosion tends to occur in the periphery of grains with relatively high stored energy (dislocation density) due to the galvanic coupling between the Cu-rich grains and the grain boundaries. Cu tends to segregate at dislocations, which leads to high amount of Cu inside the grains with high stored energy and, thus, intergranular attack is not confined to the grain boundaries, but tends to propagate further into the neighbouring grains with increased dislocation density.

Regarding the AA2198 alloy, higher degrees of pre-stretching induced fatigue life and damage tolerance improvement, as achieved for 3 % pre-stretching level and ageing for 15 h at 155 °C [52]. Recent studies concerning pre-stretching and corrosion of Al alloys [53], showed that pre-stretching impedes the formation of grain boundary precipitates and precipitate free zones (PFZs) along the grain boundaries. This is a result of dislocation-assisted nucleation of precipitates within the grains and intergranular corrosion (IGC) attack is therefore significantly reduced.

In the present work, the effect of pre-stretching on the corrosion behaviour of AA2198-T8 is investigated. Simulation of the effect of additional axial pre-stretching, after sheet production, applied during the assembly processes of aircraft parts, is attempted. The corrosion-induced degradation of the alloy's mechanical properties after pre-stretching to various levels is examined, and a quantitative estimation of ductility decrease is established. A comparison with respect to the mechanical property degradation was set against the conventional AA2024-T3, which is widely used in the aeronautical industry, to investigate the superiority of AA2198 regarding corrosion resistance. The results are interpreted by referring to dislocation-precipitate interactions.

2. Materials and experimental set up

2.1. Materials

Commercial wrought aluminium alloys (AA) 2198-T8 and 2024-T3 were used in the present study. They were received in sheet form of 3.2 mm nominal thickness from Constellium. According to the sheet manufacturer, the chemical composition of AA2198 is a combination of the following elements as percentage by weight; 2.9–3.5 % Cu, 0.8–1.1 % Li, ≤0.35 % Zn, ≤0.5 % Mn, 0.25–0.8 % Mg, 0.04–0.18 % Zr, ≤0.08 % Si, 0.1–0.5 % Ag, ≤0.01 % Fe and Al remaining. The respective composition of AA2024 is a combination of the following elements as percentage by weight; 4.35 % Cu, 1.50 % Mg, 0.64 % Mn, 0.50 % Si, 0.50 % Fe, 0.25 % Zn, 0.15 % Ti, 0.10 % Cr, 92.01 % Al. The T3 condition

refers to a solution heat-treatment performed at between 488 and 499 °C, which is followed by a water quench (max 43 °C) before cold-working and natural aging at ambient temperatures (25 °C) to a substantially stable condition [54]. The T8 temper corresponds to under-ageing condition for AA2198, since it does not possess the highest tensile strength properties during artificial ageing (peak-ageing condition) and had an appropriate artificial ageing heat-treatment from the T3 temper, as was also shown in a previous publication by Charalampidou et *al.* [55]. Sheet type tensile specimens (in accordance with the ASTM E8 [56] standard) and small rectangular coupons were machined from the longitudinal (L) rolling direction. The geometrical dimensions of the tensile specimens were 12.5 × 3.2 mm at the reduced cross section with total length of 155 mm, shown in Fig. 1(a). The rectangular coupons had dimensions 10 x 20 × 3.2 mm.

2.2. Experimental procedure

2.2.1. Pre-stretching procedure

Fig. 1(b) depicts schematically the flow chart of the experimental procedure while Table 1 presents the code names and abbreviations used throughout the manuscript for the different experimental cases. As a first step, specimens of AA2198-T8 and AA2024-T3 were machined from the sheets according to the ASTM E8 standard [56]. Tensile coupons were subsequently axially pre-stretched in a 100 kN Instron 8801 servo-hydraulic test system to specific levels of total strain (elongation to fracture, A_T) and then performed unloading to zero load. Tensile tests were carried out according to the ASTM E8 standard [56] and the strain rate was kept constant at 0.833 sec^{-1}. The applied axial strain was measured using an external extensometer attached to specimen's surface at the reduced cross-section gauge length.

The pre-stretching simulation step was programmed to bring the tensile specimens to specific fractions of the uniform elongation (A_g). Three different pre-stretching levels were selected for the present investigation, corresponding to low, medium, and high plastic deformation level for mechanical processing of aeronautical aluminium alloys. However, due to the difference in the plastic response of the two alloys considered, the selected pre-stretching levels were different for each alloy as the elongation at fracture A_f is approximately 12 % for AA2198-T8 and 19 % for AA2024-T3. Consequently, A_g is 9 % and 15 % respectively, as shown in Fig. 2. The selected pre-stretching levels were selected at 1.5 %, 4.0 % and 7.5 % for AA2198-T8 and 2.0 %, 5.0 % and 10 % for AA2024-T3 (see Figs. 2 and 3). Finally, the pre-stretched specimens were directly analysed through microscopic techniques and afterwards tensile tested to fracture, while the rest of the specimens were corrosion exposed and subsequently analysed through microscopic techniques and tensile testing to investigate the effect of pre-stretching on corrosion initiation and propagation mechanisms.

Table 1
Code names for the different experimental cases and materials used in the manuscript.

Code name	Material	Treatment	Post-treatment
2198-T8	AA2198-T8	no pre-stretching	no post treatment
2198-T8-2h_EXCO	AA2198-T8	no pre-stretching	Exfoliation corrosion (EXCO) for 2 h
2198-T8-1.5 %ps	AA2198-T8	1.5 % pre-stretching	no post treatment
2198-T8-1.5 %ps-2h_EXCO	AA2198-T8	1.5 % pre-stretching	Exfoliation corrosion (EXCO) for 2 h
2198-T8-4.0 %ps	AA2198-T8	4.0 % pre-stretching	no post treatment
2198-T8-4.0 %ps-2h_EXCO	AA2198-T8	4.0 % pre-stretching	Exfoliation corrosion (EXCO) for 2 h
2198-T8-7.5 %ps	AA2198-T8	7.5 % pre-stretching	no post treatment
2198-T8-7.5 %ps-2h_EXCO	AA2198-T8	7.5 % pre-stretching	Exfoliation corrosion (EXCO) for 2 h
2024-T3	AA2024-T3	no pre-stretching	no post treatment
2024-T3-2h_EXCO	AA2024-T3	no pre-stretching	Exfoliation corrosion (EXCO) for 2 h
2024-T3-2.0 %ps	AA2024-T3	2.0 % pre-stretching	no post treatment
2024-T3-2.0 %ps-2h_EXCO	AA2024-T3	2.0 % pre-stretching	Exfoliation corrosion (EXCO) for 2 h
2024-T3-5.0 %ps	AA2024-T3	5.0 % pre-stretching	no post treatment
2024-T3-5.0 %ps-2h_EXCO	AA2024-T3	5.0 % pre-stretching	Exfoliation corrosion (EXCO) for 2 h
2024-T3-10.0 %ps	AA2024-T3	10.0 % pre-stretching	no post treatment
2024-T3-10.0 %ps-2h_EXCO	AA2024-T3	10.0 % pre-stretching	Exfoliation corrosion (EXCO) for 2 h

2.2.2. Corrosion exposure

Prior to corrosion exposure, the side-surfaces: (i) thickness direction (TD); (ii) rolling direction (RD); and (iii) normal direction (ND), according to Fig. 1 of tensile coupons and the exposed surfaces (large surfaces parallel to rolling direction, RD-TD schematic in Fig. 1, of small rectangular coupons were ground up to 1200 grit with SiC paper, rinsed with deionized water and acetone, and finally dried at room temperature (RT) according to ASTM E8 [56] and ASTM G1 standards [57]. Grinding and cleaning are necessary processes in order to avoid heterogeneity on the materials surface and to remove any impurities, which accelerate corrosion in the micro- or macroscopic surface irregularities (claws).

For the case of tensile specimens, further preparation was required prior to their immersion to the relevant exposure environment. The preparation included shielding of specimens' surfaces so that only

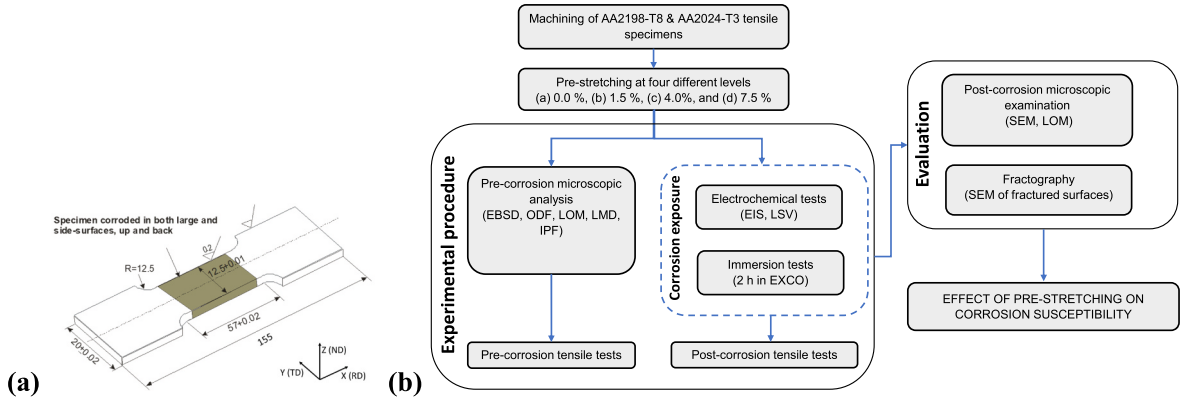

Fig. 1. (a) Schematic representation of tensile specimens according to ASTM E8 specification [56]. Grey area represents the exposed surface to corrosion attack. Orientations used during XRD studies are included and (b) experimental procedure flow diagram of the present investigation.

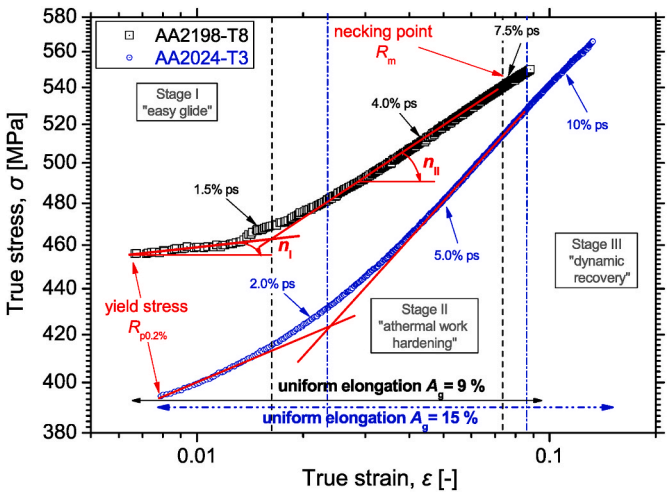

Fig. 2. Calculation of the three work hardening stages in AA2198-T8 (black hollow rectangulars) and AA2024-T3 (blue hollow circles) tensile specimens.

specific areas of interest (reduced cross-section) were exposed. Masking with appropriate insulating polyvinyl chloride PVC tape (with excellent adherence) was performed to avoid crevice corrosion beneath the masking tape. The exposed area was within the reduced cross-section to ensure fracture within gauge length, as indicated with grey colour in Fig. 1. The laboratory exfoliation corrosion environment (hereafter referred to as EXCO solution) was selected for this case, prepared according to the ASTM G34 standard [58]. EXCO solution consisted of the following chemicals diluted in 1 l distilled water: (a) sodium chloride (4.0 M NaCl), (b) potassium nitrate (0.5 M KNO_3) and (c) nitric acid (0.1 M HNO_3). Solution volume was calculated per exposure area of specimens and was 20 ml/cm^2 for all specimens, while solution temperature was 25 ± 1 °C. The specimens were then placed into containers and allowed to be exposed for 2 h to the corrosive solution. This solution was selected for time savings since it is an aggressive solution, which better simulates the exfoliation corrosion of aeronautical 2xxx and 7xxx series Al alloys [58]. It has been found that 24 h exposure of AA2024-T4 to EXCO solution corresponds to approximately 6 years of natural exposure of the same structural element regarding mass loss [59]. This short exposure time period (2 h) was chosen according to the findings of previous studies of the authors [60] where no significant surface deterioration and pitting attack was noticed, while for higher exposure times surface corrosion products were formed, which led to significant degradation of surface condition and mechanical properties 61,62. After corrosion exposure, the tensile specimens were immediately cleaned with acetone according to ASTM G34 standard [58] and then subjected to tensile mechanical testing at RT. At least three (3) specimens in each test series were used for the reproducibility of the results.

Additionally, electrochemical measurements were performed on reference (non-pre-corroded) specimens for the investigation of corrosion mechanism. Electrochemical impedance spectroscopy (EIS) as well as linear sweep voltammetry (LSV) tests were performed in a typical three electrode cell system composed of a Pt mesh as counter electrode, a saturated Ag/AgCl electrode used as reference electrode and a polished small rectangular specimen of the investigated AA2198-T8 Al alloy as working electrode which are the common minimum requirements for electrochemical tests [63]. The exposed area of specimens was 0.5 cm^2 since 0.5–1 cm^2 are the common test areas [63]. A PalmSens4® potentiostat was used for all measurements. The EIS measurements were selected since this method provides analysable information at each frequency while it allows for the determination of real surface areas in situ. The electrolyte was 3.5 % *wt.* NaCl (aq.), naturally aerated at RT = 25 ± 1 °C. This solution was selected since the in-service obtained corrosion damage correlates well to that caused by this solution [64]. Initially, the open circuit potential (OCP) was measured by recording values with 1 s interval for 30 min where stability was achieved. The OCP selected for the EIS measurements was - 0.6 V, which is the value where it was stabilized. EIS measurements were performed in a frequency scan range from 10^5 Hz down to 0.01 Hz, 10 mV (rms) voltage perturbation range and 10 points per decade acquisition rate. The measurements were repeated at fixed intervals of 0 (after 5 min immersion), 1, 3, 6, 12, 24, and 48 h of immersion time with rest periods at OCP between the measurements, in an increasing equilibration time. In parallel, LSV measurements were performed on a second, identical sample. LSV tests started after the OCP measurement in the range from −0.5 V vs. OCP to +1.5 V vs. OCP with a voltage scan rate of 0.2 mV/s. The obtained data were fitted employing PStrace5® analysis software. Each test was performed at least three times to evaluate the reproducibility of the results.

2.2.3. Mechanical tests

Tensile tests were carried out at RT using a 100 kN servo hydraulic Instron 8801 test system. Tests were performed in accordance with the ASTM E8 standard [56] and with a constant crosshead displacement rate of 0.7 mm/min. An external Instron extensometer with 50 mm ± 10 mm maximum travel was attached at the reduced cross-section gauge length of the specimens. A data logger was used during all tensile tests and the values of mechanical load, displacement and axial strain were recorded and stored in a computer. More than three (3) specimens were tested in each different case to get reliable average data. The raw data from each test were then analysed using a specially programmed Excel spreadsheet and edited with the aid of Microcal Origin© 8.5 software.

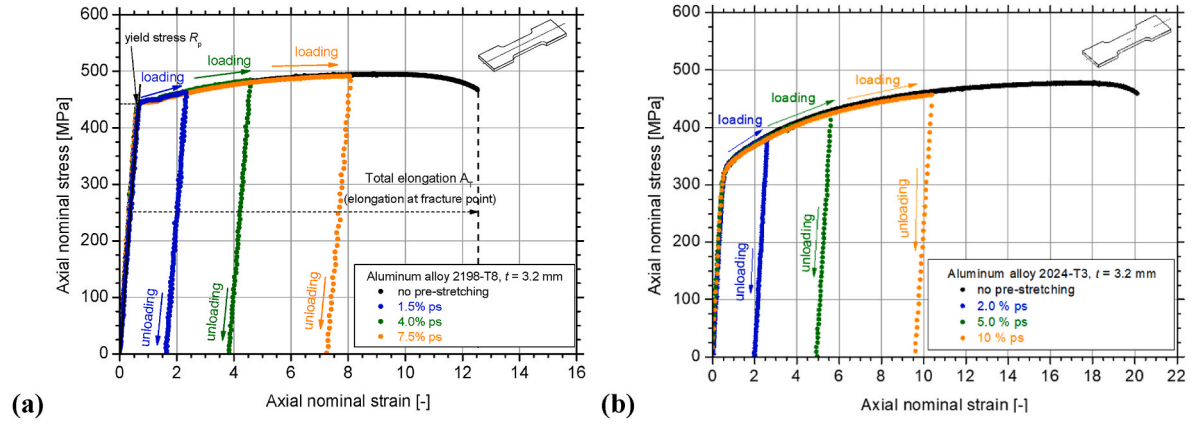

Fig. 3. Typical axial nominal stress – strain curves showing the pre-stretching process through loading – unloading steps to different investigated strain levels for (a) AA2198-T8 and (b) AA2024-T3.

2.2.4. Electron backscatter diffraction analysis

EBSD was used to analyse the effect of pre-stretching on deformed structures. Examined samples were first cold mounted and ground to 3 mm in thickness. Following grinding to a 1200 grit, samples were mechanically polished with a 3 μm solution and finished with a colloidal silica solution. Following mechanical polishing, samples were electro polished with A2® solution. EBSD acquisition was performed at a working distance of 20 mm, at an accelerating voltage of 20 kV and tilt of 70° on a JEOL IT300LV SEM equipped with an Oxford Nordlys Nano EBSD detector. Step sizes were typically around 0.4 μm unless specified otherwise. Post-processing was conducted on Channel 5 HKL software. Analyses were conducted on the RD-ND plane as depicted in Fig. 1. Analyses were completed close to the edge of the ND plane as corrosion is seen to be a phenomenon originating at the surface of the sheet material.

EBSD data were used to produce texture maps, local misorientation maps, misorientation angle distribution data and orientation distribution functions. For Al alloys with face-centered cubic (FCC) structures, the orientations of specific interest, are shown in Table 2. Preferred orientations essentially have their resultant effects on the macroscale properties of material, such as strength properties and ductility. For instance, at low deformation, α-fibre texture, with {011}//ND prevail in FCC metals such as Al alloys. This varies from Goss texture with {011}⟨100⟩ to Brass texture with {011}⟨211⟩. Under higher deformation schedules, β-fibre texture prevails which varies from Copper {112}⟨111⟩ through S {123}⟨634⟩ to Brass orientations {011}⟨211⟩ [65–67].

Furthermore, local misorientation mapping (LMM), and orientation distribution function (ODF) were also basic constituents of the EBSD analysis. LMM displays minute orientation changes within a material's structure to relate it to the deformation of structure. The process calculates the misorientation of a pixel relative to surrounding pixels and states the average misorientation of the pixel relative to its neighbours [68]. ODFs are useful in identifying textures present in a sample analysed. These maps represent the frequency of specific orientations being present [69].

2.2.5. Scanning electron and light optical microscopy

Specimens were sectioned from the as-received AA2198-T8 material for microscopy. The samples were sectioned and cold mounted such that the L-T plane could be investigated. Following grinding (1200 grit) and polishing with a 1 μm solution, the samples were etched with Dix-Keller's reagent (190 ml distilled water, 5 ml HNO_3, 3 ml HCl and 2 ml HF) for different exposure times. The samples were first analysed using an Olympus BX51 M light optical microscope, followed by scanning electron microscopy (SEM) using a Zeiss 540 Ultra high resolution FEG-SEM at an excitation voltage of 10 and 20 kV.

SEM analysis of the fracture surfaces and exposed surface of the tensile specimens were performed after fracture, with the aim to evaluate the effect of pre-stretching on the corrosion and fracture behaviour of the AA2198-T8 alloy, due to short-term EXCO exposure. The Zeiss 540 Ultra high resolution FEG-SEM was used at an excitation voltage of 20 kV for these investigations. Thereafter, a Future-tech FM-700 microhardness tester – with a micrometer controlled, moveable X–Y stage/holder – was used in order to measure the secondary crack widths and the distance of the cracks from the fracture surface.

3. Results

3.1. Microscopic analysis of pre-stretched specimens

Fig. 4(a) shows the microstructure of AA2198-T8 prior to corrosion exposure. In general, the microstructure comprised of an elongated grain structure that reflects the rolling direction. Near the external surfaces, however, a tendency towards a more equiaxed structure is observed as shown in Fig. 4(b). Such a change in microstructure may result in differences in the corrosion resistance of the external and internal structure. An example of such changes was given by Araujo et *al.* [70], in which the corrosion behaviour of different tempers of Al alloy 2198 was investigated. Although so-called severe localized corrosion (SLC) was proposed to exist in both the pre-stretched T851 and T8 tempers, the propagation of corrosive attack was found to be different in the two conditions. In the case of the cold worked T8 temper, Araujo et *al.* [70] proposed that variations in the amount of deformation within given grains would result in variations in the fraction of T_1 phase precipitation. Therefore, grains with higher degrees of deformation would have higher densities of T_1 phase and are believed to be more reactive. As such, these grains would act as the anode, whilst the surrounding (less deformed) grains would act as the cathode, resulting in the selective dissolution of the highly deformed grains. Nevertheless, in the case of the T851, selective dissolution of the slip-bands (anodic) is believed to occur intra-granularly. This is due to creation of slip-bands inside grains during pre-stretching, and the selective precipitation of the T_1 along these bands [70].

Evidence of dissolution of the more reactive (highly deformed) grains within T8 temper may also be seen after etching the sample with Keller's reagent, *e.g.*, the optical micrographs in Fig. 4(a) and (b) as well as the SEM micrograph in Fig. 4(c). That is, the corrosive attack due to exposure of AA2198-T8 to the etchant appears to have selectively dissolved some of the grains (yellow arrowed in both figures), whilst other grains appear to be less corroded. This is especially evident from a fuzzy surface appearance in the under-etched sample shown in Fig. 4(c). It is noted that this surface appearance is observed to a higher degree within the dissolved grains. Considering the corrosion mechanisms described by Araujo et *al.* [70], the speckled appearance is probably a result of localized etchant-induced corrosion of the hardening precipitates (*i.e.*, δ' or T_1), in the vicinity of which corrosion (or corrosion products) is observed. Micrometric constituent intermetallic particles (phases) were also observed during SEM microscopy and energy dispersive spectroscopy (EDS) mapping (the bright constituents in the SEM micrograph of Fig. 4(c). These particles were found to comprise of Cu and/or Fe and are represented in various sizes and morphologies. These observations are in good correlation with the work by Araujo et *al.* [70]. In the presence of a corrosive atmosphere, these particles will create micro-galvanic couplings with the surrounding matrix acting as the anode. Ultimately, this

Table 2
Important orientations, properties and portrayal of colour used for aluminium as used in discussion at Fig. 5 [65], [66].

Designation	Dominant Miller Indices {hkl}⟨uvw⟩	Characteristics	Colour used in texture map
Goss	{011}⟨100⟩	β-fibre component. Results from Brass after breakdown of Brass texture following deformation or recrystallisation	
Copper	{112}⟨111⟩	β-fibre component. Formed after recrystallisation of Brass	
Brass	{011}⟨211⟩	β-fibre component. Typically found in deformed materials after thermomechanical processing	
S	{123}⟨634⟩	Typically found in deformed materials	
Cube	{001}⟨100⟩	Formed after recrystallisation of Brass	

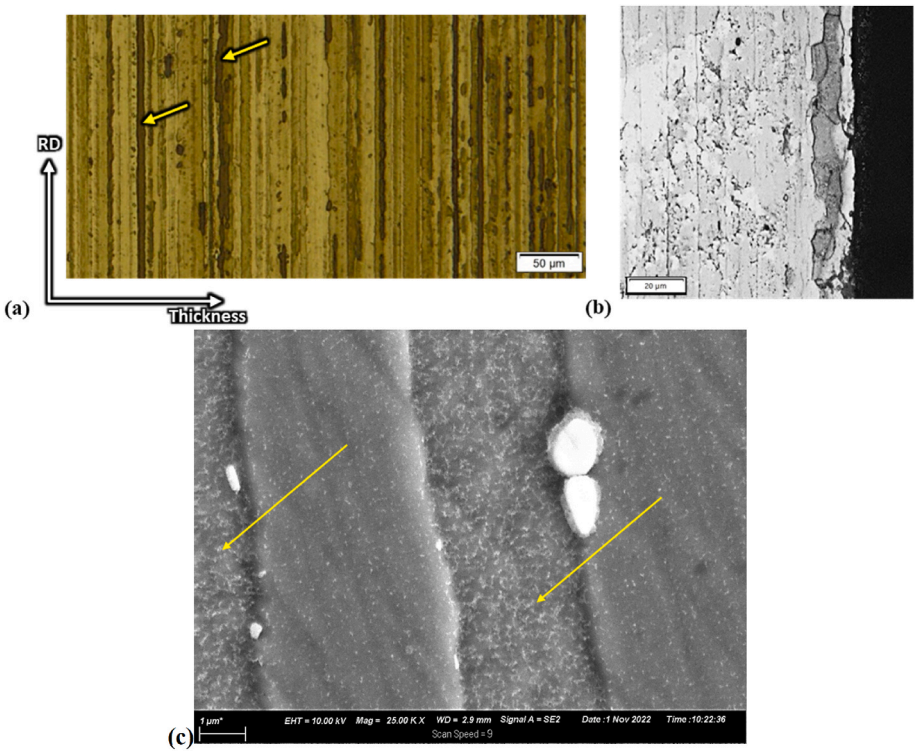

Fig. 4. Optical micrographs summarizing the grain morphologies of etched AA2198-T8 in cross-section; (a) at a location away from the outer exposed surface, (b) at the exposed surface (etchant: Keller's reagent, 30 s exposure) and (c) SEM micrograph, showing the selective dissolution of some grains after short term exposure to Keller's reagent.

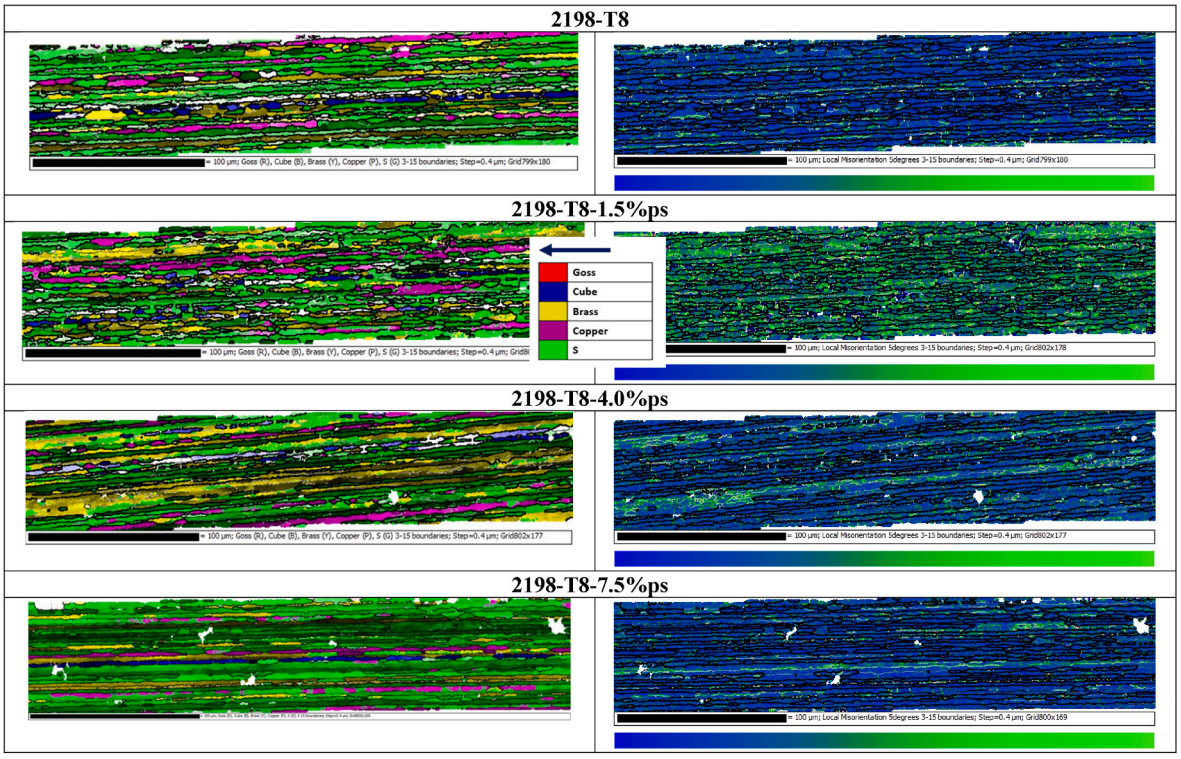

Fig. 5. Textural maps (left micrographs, with corresponding colour legend, see also Table 2) and local misorientation intensity (varies between 0° represented by blue colour to 2° represented by green colour) maps (right micrographs) of AA2198-T8 for the reference T8 temper as well as for the three different investigated pre-stretching levels. Imaging along the RD-ND plane.

will result in trenching around the particles, and localised corrosive attack.

3.2. EBSD analysis of pre-stretched specimens

Following EBSD analysis, textural maps were produced and are presented in Fig. 5 (left micrographs). They show a dominance of yellow and green colours for various grains, which correspond to Brass-type and S-type texture respectively (see Table 2). The elongated grains have bands of Cube, Copper and Goss-type grains but are dominated by the Brass and S textures. It is noted that the dominance of Brass- and S-type textures is typical of highly deformed structures 65–67. Holroyd et *al.* [71] also mentions that random equiaxed orientations favour intergranular corrosion whilst elongated structures favour exfoliation of grains. Areas that are shaded in white on texture maps are generally characterised as not aligning to a specific textural orientation.

Deformation maps in the form of local misorientations are shown in Fig. 5 (right micrographs), where a blue colour represents no misorientation (0°) and green represents a misorientation of 2°. As the as-received sample is already cold worked, the reference sample is found to also have some misorientation distributed within the sample as shown by the distribution of green colour in the sample. A close observation of Fig. 5 (left and right) shows that the reference sample had deformation concentrated in S oriented grains (on texture maps), whilst in the pre-stretched samples, strain/deformation was more concentrated in the Brass-type grains.

As the step sizes are consistent and the areas analysed are relatively large, the local misorientation maps in Fig. 5 (right micrographs) can be compared effectively. It is found that for the 2198-T8-1.5 %ps sample, the local misorientation map has misorientation scattered throughout the map area, whilst for the other cases, 2198-T8, 2198-T8-4.0 %ps and 2198-T8-7.5 %ps, deformation is concentrated in smaller regions and within specific grains. This observation is believed to be significant, indicating that pre-stretching beyond 1.5 % could be linked to some form of recovery in the samples, allowing for dislocations to re-organize within the structure [72].

Misorientation angle distribution (MAD) data give an idea of misorientation within a sample. These can be classified as correlated or uncorrelated data. Uncorrelated data are taken for misorientations relative to a random starting point, correlated data are taken for misorientation between neighbouring points of data. As correlated data give misorientation between adjacent points, it can be analogous for grain boundary identification. It is seen from the correlated data in Fig. 6 (a) and (b), that the non-deformed sample (2198-T8) has a higher amount of low angle grain boundaries (LAGBs), and substructure relative to that of the sample stretched at 7.5 % (2198-T8-7.5 %ps). The intensity of the low angle misorientation in 1.5 % pre-stretched sample shows that the entire structure has a high proportion of LAGBs misorientations (shown in light green bar in the correlated MAD data). The correlated misorientation distribution of the 4.0 % and 7.5 % pre-stretched samples (Fig. 6(b)) shows an even distribution of misorientations typical of recovery in the samples due to increased deformation [72].

Fig. 6(c) shows the cumulative distribution of MAD of different grain

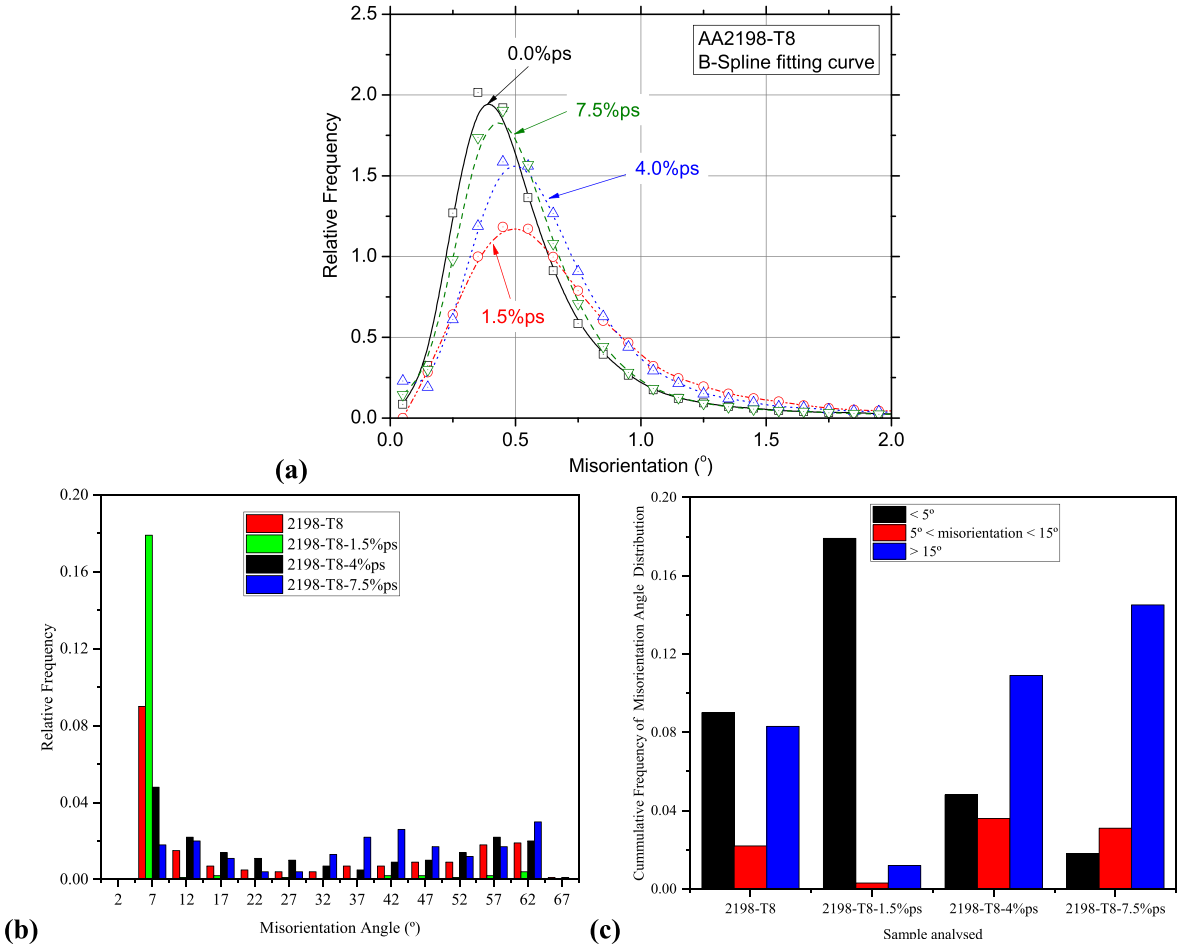

Fig. 6. (a) Local misorientation distribution at the edge of the specimen with correlating intensity scale for local misorientation distribution, (b) correlated misorientation angle distribution at the edge of the specimens and (c) cumulative grain boundary orientations taken from (b) for the investigated pre-stretching levels of AA2198-T8.

boundaries as a function of the pre-stretching level. These data were taken from the correlated MAD data in Fig. 6(b). The figure shows a transition to HAGBs structure with increasing the pre-stretching level beyond 1.5 % to the 7.5 % pre-strained sample. This increase in the amount of HAGBs is typically due to occurrences such as continuous dynamic recovery and/or recrystallization 72,73. Previous research [74] has shown that an increased proportion of HAGBs leads to an increased corrosive susceptibility.

The orientation density function (ODF) analysis presented in Fig. 7 shows that the dominant texture present within the sample (mid-thickness) is a Brass texture arrowed in red with the presence of an S texture arrowed in white. This corresponds to the texture maps plotted previously showing the dominance of yellow- and green-coloured grains correlating to Brass and S texture, respectively. Work by Zhang et *al.* [75] on an Al–Li alloy has shown that surface grains and orientations could be equiaxed with Cube, Brass and Cu textures due to shearing from processing during extrusion.

The general grain structure of the material is elongated, with the typical orientation being consistent with Brass and S orientations. Naturally, an increase in deformation resulted in an increase in misorientation and dislocation density within samples. The presence of Brass and S textures are typical of highly deformed structures. This is also evident by the increased intensity of the S texture for the 7.5 % pre-strained sample shown in Fig. 7.

3.3. Corrosion results of pre-stretched specimens

Electrochemical impedance spectroscopy (EIS) results for AA2198-T8 in different pre-stretched levels are shown in Fig. 8 in the form of Nyquist and Bode plots. Well-defined capacitive loops are noticed in all investigated cases. One capacitive loop is noticed in high frequencies regime, for all exposure times and all cases, which corresponds to the flat surface oxide film while a Warburg element is noticed in low frequencies regime. Nonetheless, distinct differences still exist. For the non-pre-stretched samples, the impedance values (capacitive loop, semi-circle arc) fluctuates with immersion time as presented in Fig. 8(a_1), while for those pre-stretched at 1.5 % ps level, see Fig. 8(b_1), the impedance values climb up to 12 h and then for higher exposure times are significantly decreased. For higher pre-stretched levels (*i.e.*, 4.0 % and 7.5 %) the impedance values climb up to 6 h and then degrade; but this degradation is lower than the one presented in non-pre-stretched samples. Nevertheless, the values for the non-pre-stretched samples are one order of magnitude higher from those of pre-stretched. The phase angle vs. frequency plots revealed one time constant at low frequencies (10^{-2} to 10^{-1}) and one at medium frequencies (10^{0} to 10^{3}), respectively. Time constants distributing at medium frequencies are correlated to charge transfer procedures coupled with the double layer capacitance [70], [76], while those at low frequencies, accompanied with a low slope of the impedance modulus at low frequencies, are likely to be related to diffusion-controlled corrosion processes. The results for 2198-T8 specimens, *e.g.*, Fig. 8(a_2), which were taken from a previous paper of the authors [61], revealed a general decreasing trend for the impedance modulus |Z| with increasing immersion time to 3.5 *wt* % NaCl solution and after 1 h of immersion; nevertheless, it was not significantly reduced for the short exposure times and up to 3 h. A significant sudden drop of the impedance modulus was noticed after 6 h, followed by a gradual decrease for higher exposure times. However, the gradual decrease between exposure times was diminished at high exposure times and after 12 h due to the formation of stable pits and control of the corrosion process by the diffusion-limited cathodic oxygen reduction. The decrease of impedance modulus |Z| in the middle and low frequencies regime was accompanied by a decline of the phase angle and shift of relaxation process towards lower frequencies (*i.e.*, from $\approx 10^{2}$ to 10^{1}). This can be correlated to a loss of the capacitive behaviour on the specimen's surface when the system is highly kinetic and consequently to a total decreased corrosion resistance.

Regarding the pre-stretched specimens, the EIS spectra showed that |Z| was lowered when compared against the non-pre-stretched specimens (AA2198-T8). However, the effect of corrosion exposure and immersion increasing time was diminished, with the lowest differences between the curves of different exposure times to be noticed for 2198-T8-1.5 %ps specimens. Nonetheless, a shift of time constants towards lower frequencies with increasing exposure time was noticed for all pre-stretched levels, revealing a decreased corrosion resistance.

To gain a better insight into corrosion mechanisms, in order to define the differences between the results of various pre-stretched levels of AA2198-T8, EIS response is modelled using equivalent electrical circuits. The circuit fitting was performed on PSTrace® software, from which several circuit models were chosen according to the electrochemical impedance spectroscopy response of each condition. The circuit model with the lowest Chi-Squared value and low error values of each parameter involved was selected for further analysis. The chosen model is shown in Fig. 9, and the fitting results are presented in Fig. 10, showing the data fitting for the pre-stretched samples of AA2198-T8 after 1 h exposure to 3.5 % *wt*. NaCl solution. From the equivalent electrical circuit model several useful parameters were calculated such as R_1 element, which represents corrosive medium resistance, and the pair $R_2//Q_1$, representing the resistance of electron flow through double layer in parallel with capacitance of double layer, *i.e.,* the charge held in the double layer interface. A constant phase element (CPE) – that is denoted with Q in the present work – was used instead of an ideal capacitor to take into consideration the heterogeneity of the surface, as

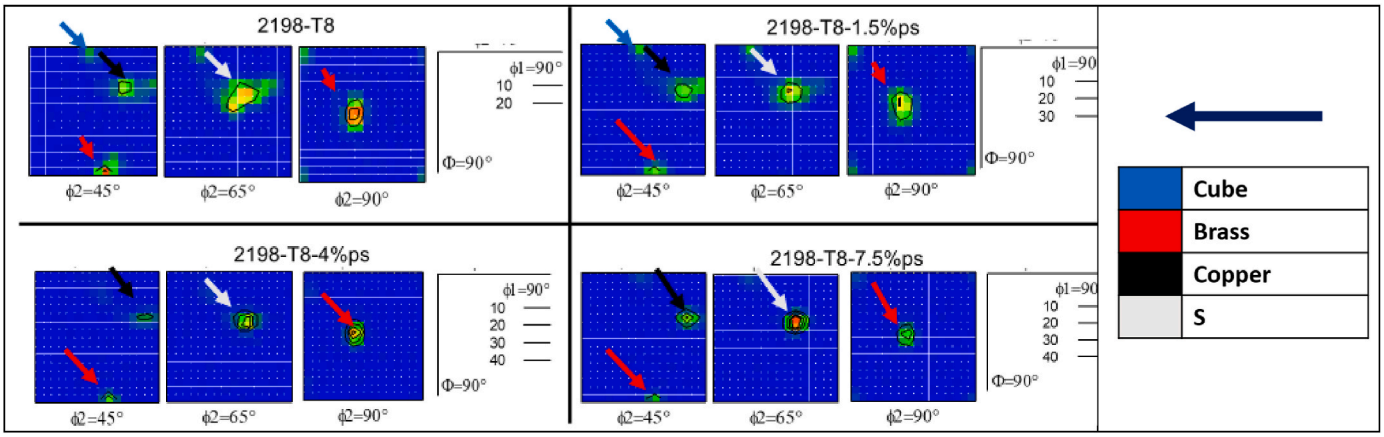

Fig. 7. Orientation density function (ODF) maps showing the relevant sections for the sample edge, with legend of arrow colours highlighting specific textures of interest.

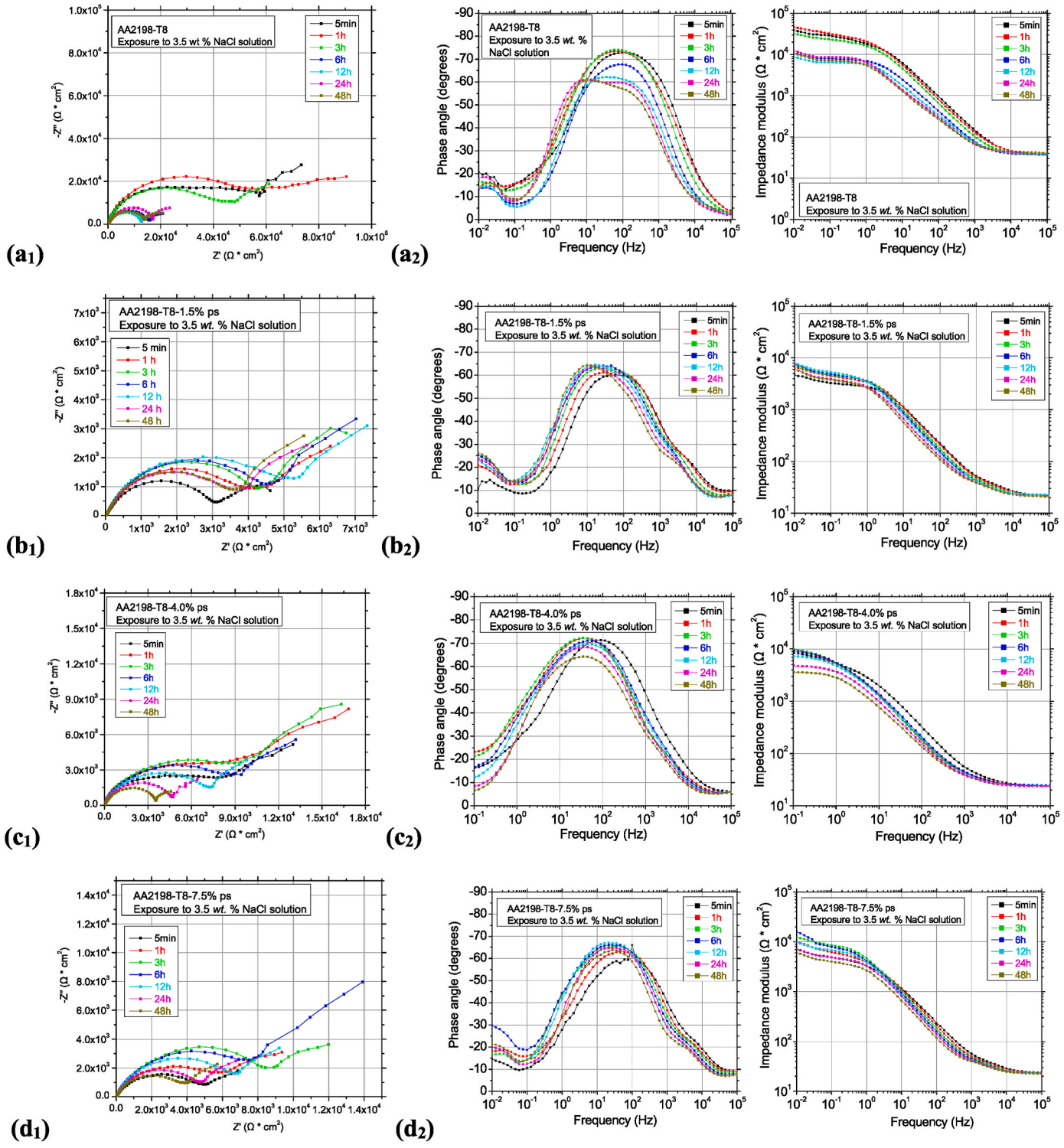

Fig. 8. Impedance spectra of AA2198-T8 exposed to 3.5 % *wt.* NaCl (aq.) for various times and for the samples (a) 2198-T8, (b) 2198-T8-1.5 %ps, (c) 2198-T8-4.0 % ps and (d) 2198-T8-7.5 %ps.

already mentioned in literature [77]. Additionally, a Warburg *W* impedance element was added to the model, to better correspond to the response at low frequencies as they are being controlled by diffusion-controlled processes. A Warburg element is a parameter used to model the charge transfer between the electrode and redox species in the corrosive medium as well as the depletion of the diffusion layer in systems of semi-infinite diffusion. In contrast to the Warburg element the Warburg open/short does not assume semi-infinite diffusion. The Warburg open (T) model, used in the present case, is representative of systems with reflective boundaries of a diffusion layer and are applied when a finite length diffusion layer is assumed.

The charge transfer (R_{CT}) resistance (R_2 in the electrical circuit model) was selected for further investigation, since it represents the resistance of electron flow through double layer, thus the specimen's corrosion resistance. As can be seen from Fig. 9, the pre-stretching process results in decreased charge transfer resistance. This

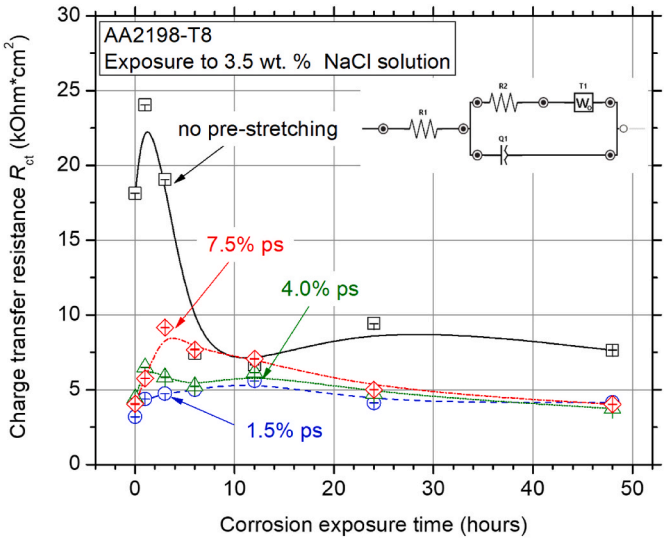

Fig. 9. Charge transfer resistance (R_{CT}) derived from EIS data fitting vs. corrosion exposure time for AA2198-T8 specimens pre-stretched at various strain levels.

degradation is attributed to the higher amount of deformation, which leads to increased dislocations and consequently increased volume fraction of naturally-aging second-phase precipitates (such as δ in this alloy). The 2198-T8-1.5 % ps specimens exhibited the lowest charge transfer resistance throughout immersion time range, while increasing pre-stretching levels resulted in higher R_{CT} values, especially for the short exposure times and up to 12 h. Hence, it seems that the recovered surface with higher misorientation angle of grain boundaries (higher angle grains) contributes to corrosion resistance and hinders corrosion attack initiation. Nevertheless, specimens with higher pre-stretching level seem to corrode at higher rates with increasing exposure time. What is of major interest is the high degradation rate of R_{CT} for non-pre-stretched specimens represented by the black curve, with increasing exposure time and beyond the peak resistance value. It seems that pre-stretching at low levels enhances corrosion attack susceptibility, but the corrosion propagates with lower rate in the LAGBs structures.

Fig. 10 shows the impedance plots (Nyquist and Bode) for each different pre-stretching level, i.e., 1.5 %, 4.0 % and 7.5 % ps, after 1 h corrosion exposure with the fitting curves of the chosen equivalent electrical circuit model. Good fitting results are observed in Fig. 10, which confirm that the selected equivalent electrical circuit model is the one that better simulates the corrosion mechanism of AA2198-T8 under different pre-stretching conditions.

The LSV experimental data are summarized in Fig. 11. The general asymmetric shape of the plots is similar to the respective reported by Prakashaiah et *al.* [78] for AA2024-T3. Nevertheless, more negative E_{corr} values were recorded in the present case for AA2198-T8. The asymmetrical branches (cathodic and anodic) of the curves are attributed to localized corrosion [79], thus making it difficult to quantitatively extract results. The absence of a distinct Tafel region in the cathodic branch of the curves is due to diffusion limitations of dissolved oxygen during reduction reactions as well as reduction of protons added to the diffusion-limited current of oxygen reduction, which leads to a steep increase of total current at more negative potentials. On the contrary, in the anodic region it is the oxidation of the alloy's elements, mostly oxidation of Al to its trivalent ions (Al^{3+}), which combine with O^{-2} ions produced by the O_2 reduction reaction to form the passive oxide film. It must be noted that since an intrinsic oxide layer is already present before the LSV measurements, the anodic branch has no active and passive regions as was also defined by Makuch [80], and the sharp increase of the anodic current density immediately above the corrosion potential E_{corr}, which is noticed for the non-pre-stretched samples in the present case, indicates an immediate pitting attack, confirming that the alloys are already in their breakdown potential at E_{corr} in such an aggressive electrolyte. When comparing the different pre-stretching levels of AA2198-T8, it can be noticed that there are several differences. The non-pre-stretched sample presented only one clearly defined peak at $E_{corr} = -0.86$V vs. $Ag/AgCl_{sat.}$, while the three pre-stretched samples revealed this same peak and one additional peak at approx. −0.78V vs. $Ag/AgCl_{sat}$. For the first peak, the values of i_{corr} were almost the same for all four samples with slightly lower cathodic activity to be noticed for the pre-stretched specimens, while for the second peak, respective current values exhibited slight differences. This second Tafel peak is more pronounced for lower pre-stretching degrees and the fact that it appears at a more anodic potential in respect with E_{corr} suggests that, despite enhanced crack formation upon pre-stretching, simultaneously, a more corrosion-resistant phase is formed at the grain-boundaries. This more corrosion-resistant phase is possibly favourably formed inside cracks, since cracks are only present in pre-stretched samples. As it is well known, defect-richer areas, such as cracks, are more prone to corrosion and therefore corrosion products, such as oxides and hydroxides, can form in these areas in more significant amounts and locally passivate the surface. As a result, the crack areas of pre-stretched samples act as a different electrode with more anodic E_{corr}, which manifests itself as a second peak in Tafel plots. The values of the LSV measurements are shown in detail in Table 3. This observation is in accordance with the results of R_{CT} data. The higher reactivity of higher deformed specimens is also in accordance with the results by Araujo et *al.* [70] and Jinlong et *al.* [81]. Finally, no essential differences in E_{corr} were noticed since it seems to fluctuate for the different pre-stretching levels.

Overall, literature data on corrosion of 2024-T3 Al alloy in 3.5 *wt* % NaCl solution, as reported by Prakashaiah et *al.* [78], are very similar to the experimental EIS and LSV data of the present study regarding 2198-T8 alloy's untreated and pre-stretched samples. Table 4 shows all the parameters of the fitted electrical circuit model of the various pre-stretching levels of AA2198 along with three (3) different corrosion exposure times for comparison purposes. The initial increase of the derived charge transfer resistance followed by its decline, reported by Prakashaiah et *al.* [78], is in agreement with the EIS-derived R_{ct} vs. time diagrams of the present study, as presented in Fig. 9. It must be noted that the approach in the present study differs from Prakashaiah et *al.* [78] in that a different equivalent electrical circuit model is chosen (insert in Fig. 9).

3.4. *Effect of pre-stretching on corrosion-induced degradation*

Fig. 12 presents the tensile flow curves (stress-strain) of AA2198-T8 for the specimens pre-stretched at various levels (Fig. 12(a)) as well as the pre-stretched and subsequent corroded specimens (Fig. 12(b)). By comparing the two figures, *i.e.*, Fig. 12(a) and (b), higher corrosion-induced degradation of elongation to fracture was noticed for the non-pre-stretched as well as for the low level pre-stretched specimens (2198-T8-1.5 %ps) while differences in elongation to fracture are not substantial for the high level of pre-stretching. Regarding the surfaces of the EXCO-exposed specimens, several corrosion products were observed on the fractured surface at locations near the exposed surface (refer to Fig. 12(c)). Corrosion was found to extend to a depth of approximately 20 μm, where after a transition to the general fracture morphology is observed. The corrosion, however, was not found to follow the entirety of the external surface layer, as can be seen in the left figure of Fig. 12(c) showing the opposite side of the gauge section to that of the right figure. Less but not least, Fig. 12 demonstrates that both an increased yield stress (represented by $\Delta\sigma_0$) and extended Stage I work hardening ("easy-glide") region are observed after the 1.5 % pre-stretching operation. The combination of these two observations is an indication of a Lüders strain mechanism, as observed in other Al alloys [82]. It seems that at low pre-strain levels, the movement of newly generated dislocations are hindered by some means, resulting in the increased yield stress. With

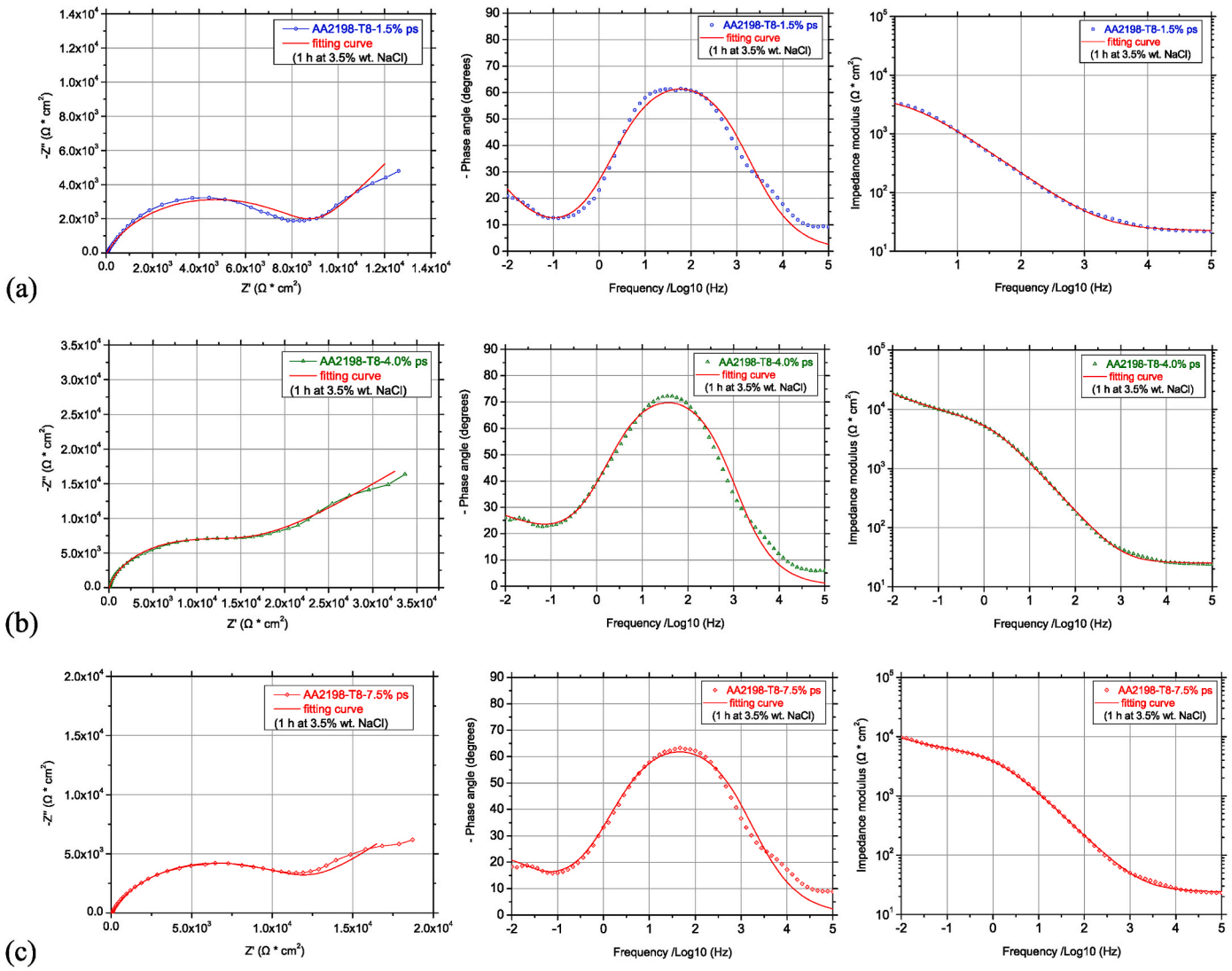

Fig. 10. Plots of EIS spectra of AA2198-T8 pre-stretched specimens exposed to 3.5 % *wt.* NaCl (aq.) solution for one (1) hour with the fitting curves (red lines) of the chosen equivalent electrical circuit model included for the samples of (a) 1.5 % ps, (b) 4.0 % ps and (c) 7.5 % ps level.

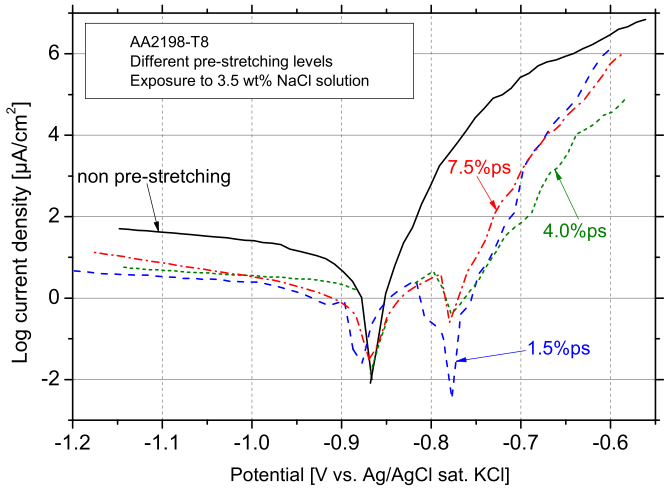

Fig. 11. Tafel plots from LSV measurements in 3.5 % wt. NaCl (aq.) electrolyte with 0.2 mV/s scan rate for AA2198-T8 specimens pre-stretched at various strain levels.

Table 3
Corrosion parameters derived from LSV measurements of AA2198 specimens pre-stretched at various strain levels.

Pre-stretching level	i_{corr} (μA/cm²)		E_{corr} (V vs. Ag/AgCl sat. KCl)		β_c (mV/decade)	
	average value	error	average value	error	average value	error
0.0 %	1.707	±0.22	−0.866	±0.045	124.235	±10.23
1.5 %	**0.665**	±0.092	**−0.879**	±0.024	29.851	±9.56
4.0 %	0.749	±0.13	−0.868	±0.061	65.236	±4.09
7.5 %	1.155	±0.91	−0.869	±0.016	41.938	±9.77

increasing applied strain in Stage I, however, the dislocations are released from the obstacles, resulting in flow at a low work hardening rate. An explanation that accounts for both the increased yield stress and the extended Stage I region is the nucleation of second phases on the dislocations generated during the pre-straining.

The experimental results of the tensile properties derived from the stress-strain curves are summarized in Fig. 13 as average values. The mechanical properties selected for further investigation were yield stress R_p and elongation to fracture A_T (as shown in Fig. 3(a)), since these mechanical properties are measures of the mechanical strength and

Table 4
Values of the EIS parameters extracted from the equivalent circuit model of AA2198-T8 in different pre-stretching levels.

Sample	1 h					6 h					24 h				
	R_1 [Ω*cm^2] (error)	R_2 [Ω*cm^2] (error)	Q_1 [T] (error)	n_1 [φ] (error)	T_1 [σ] (error)	R_1 [Ω*cm^2] (error)	R_2 [Ω*cm^2] (error)	Q_1 [T] (error)	n_1 [φ] (error)	T_1 [σ] (error)	R_1 [Ω*cm^2] (error)	R_2 [Ω*cm^2] (error)	Q_1 [T] (error)	n_1 [φ] (error)	T_1 [σ] (error)
2198-T8	38.86 (0.83 %)	2.40E+04 (4.29 %)	2.415E-6 (1.81 %)	0.856 (0.29 %)	8785 (15.9 %)	37.075 (0.63 %)	7.44E+03 (3.35 %)	5.215E-6 (1.87 %)	0.845 (0.32 %)	1591 (19.24 %)	39.865 (1.86 %)	9.42E+03 (13.54 %)	1.207E-5 (5.32 %)	0.784 (0.99 %)	751.1 (4.89 %)
2198-T8-1.5 %ps	22.08 (2.02 %)	4.39E+03 (11.61 %)	1.745E-5 (4.68 %)	0.762 (0.91 %)	1003 (17.8 %)	22.66 (1.72 %)	5.00E+03 (12.59 %)	2.077E-5 (4.34 %)	0.784 (0.86 %)	932.0 (18.30 %)	21.855 (2.28 %)	4.11E+03 (17.07 %)	2.951E-5 (5.61)	0.765 (1.18 %)	623.7 (33.86 %)
2198-T8-4.0 %ps	25.14 (1.53 %)	6.48E+03 (14.03 %)	1.141E-5 (4.54 %)	0.846 (0.83 %)	1.028E+4 (22.78 %)	24.375 (1.06 %)	5.24E+03 (15.78 %)	1.074E-5 (3.29 %)	0.841 (0.58 %)	5506 (11.93 %)	24.54 (0.91 %)	6.14E+03 (5.62 %)	1.233E-5 (2.53 %)	0.831 (0.47 %)	2401 (11.22 %)
2198-T8-7.5 %ps	23.96 (1.91 %)	5.76E+03 (6.61 %)	1.798E-5 (4.48 %)	0.760 (0.90 %)	2367 (20.50 %)	23.87 (2.19 %)	7.68E+03 (25.66 %)	2.040E-5 (6.10 %)	0.783 (1.20 %)	3560 (7.12 %)	24.01 (2.01 %)	5.00E+03 (15.65 %)	2.268E-5 (5.23 %)	0.789 (1.06 %)	792.2 (2.26 %)

tensile ductility characteristics of the material, respectively. More specifically, in Fig. 13(a) the experimental results of yield stress (left y-axis) and elongation to fracture (right y-axis) of AA2198-T8 are presented as a function of the pre-stretching level. The effect of corrosion exposure on both mechanical properties tends to decrease with increasing pre-stretching level. Nevertheless, the effect is more pronounced for elongation to fracture, where significant corrosion-induced degradation of the property is evident for 2198-T8 and 2198-T8-1.5 %ps specimens while for 2198-T8-7.5 %ps it is almost eliminated. This behaviour can be attributed to different types of corrosion attack and propagation mechanism; crystallographic corrosion attack is likely to take place at higher pre-stretched specimens rather than intergranular (IGC), which seems to be present on 2198-T8-1.5 %ps specimens due to the higher number of low-angle grains and, consequently, higher density of grain boundaries. For the 2198-T8-1.5 %ps case, for example, a high proportion of low-angle grain boundaries (LAGBs) is present, promoting nucleation of T_1 and δ' precipitates on the large surface area of these grain boundaries and formation of precipitate free zones (PFZs). Consequently, the intergranular corrosion susceptibility of this sample is high. With increasing pre-stretching, recovery takes place as was revealed from the EBSD analysis (*e.g.*, section 3.2), and the proportion of LAGBs is reduced, making for reduced total grain boundary surface area and lower intergranular corrosion susceptibility. Recovery leads to a more homogeneous distribution of dislocations in smaller regions and inside specific grains, thus promoting intragranular corrosion with deceased corrosive degradation [53], [83].

A comparison with AA2024-T3 is also included (refer to Fig. 13(b)) and it seems that the level of pre-stretching has no effect on corrosion degradation mechanism in this alloy, since the difference in corroded and non-corroded curves of the pre-stretched AA2024-T3 specimens remains relatively high and almost the same for all pre-stretching levels.

3.5. Fractographic analysis

In all the pre-stretching conditions considered, the macro-fracture behaviour is observed to be a shear failure; with the fracture surfaces oriented at a 45° angle to the applied load. The high-resolution SEM-fractography in Fig. 14 summarizes the general fracture morphology, which presents as a layered, lamella-type structure comprising of apparently featureless or smooth fracture. The apparently featureless fracture surface resembles that observed by Guo et *al.* [84], which was ascribed to intergranular delamination along the elongated grain-structure; the latter produced during the cold rolling operation. The current work corroborates these results, with some of the fractography (*e.g.*, Fig. 14(b_2) and (b_1)) revealing the underlying grain structure. Guo et *al.* [84] also showed that – although the majority of the fracture surface comprised of a delaminated fracture morphology – the layer or lamella edge comprised of a ductile (dimpled) fracture morphology when viewed perpendicular to the thickness of the specimen. However, in comparison, the current work revealed very little to no evidence of a dimpled fracture morphology at the lamella edges. Although some isolated dimpled morphologies may be seen in the case of the 2198-T8 (0 %ps) EXCO exposed specimen, no such morphology is observable for the 2198-T8-7.5 %ps condition (EXCO exposed and unexposed). Moreover, the dimpled morphology observed for the 2198-T8 (0 %ps) sample is apparently associated with the intergranular constituent particles, as was revealed in the microscopy section, and this is in accordance with the literature [85].

A possible reason for the presence of the corrosion product on the fracture surface becomes evident when considering the low magnification SEM images in Fig. 15. After the tensile testing of the EXCO-exposed specimens, extensive secondary cracking was observed throughout the different pre-stretching conditions employed but being the most severe for the 2198-T8-1.5 %ps-2h_EXCO sample, where intergranular subsurface cracking was dominant. These results support the findings of the previous sections 3.2 to 3.4 where the pronounced EXCO

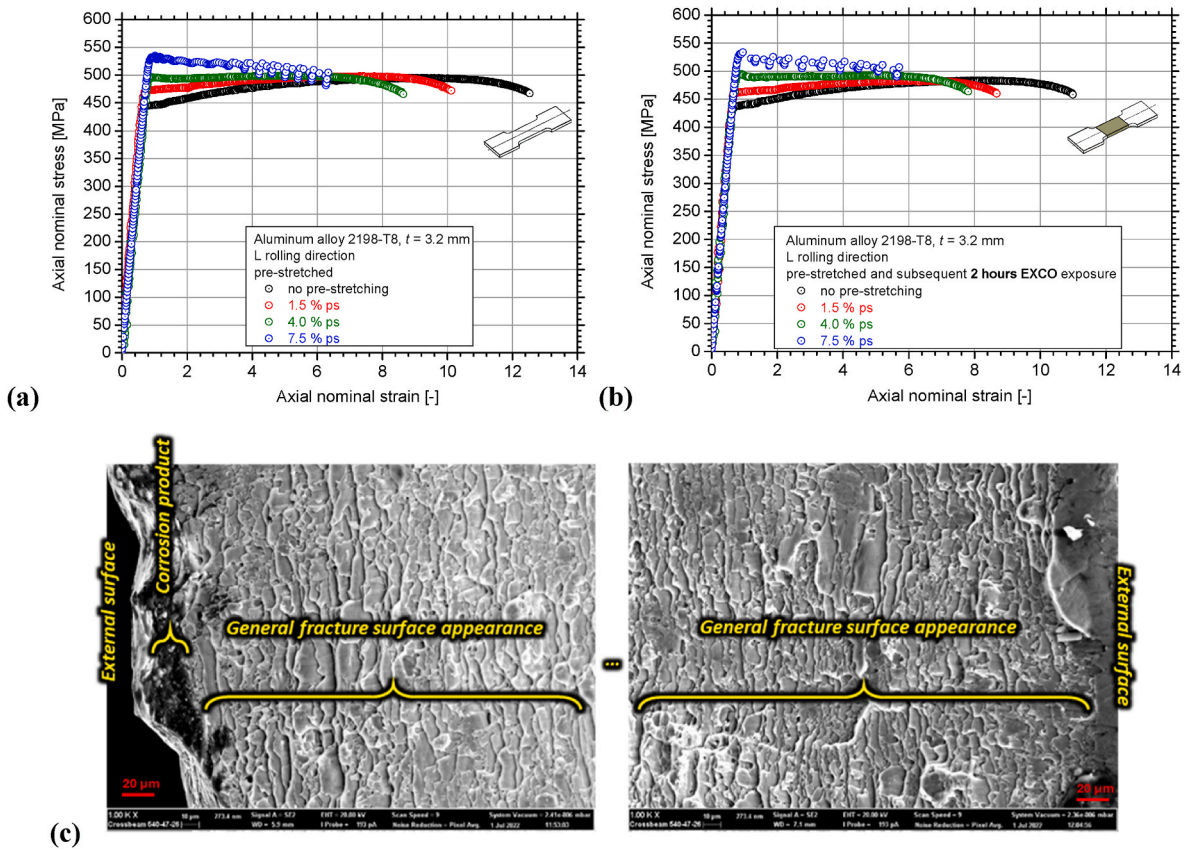

Fig. 12. Typical tensile flow curves of AA2198-T8 pre-stretched specimens for different stretching levels (a) without corrosion exposure, (b) after 2 h corrosion exposure to EXCO solution and (c) SEM-fractographs of the 2198-T8-2 h_EXCO specimen.

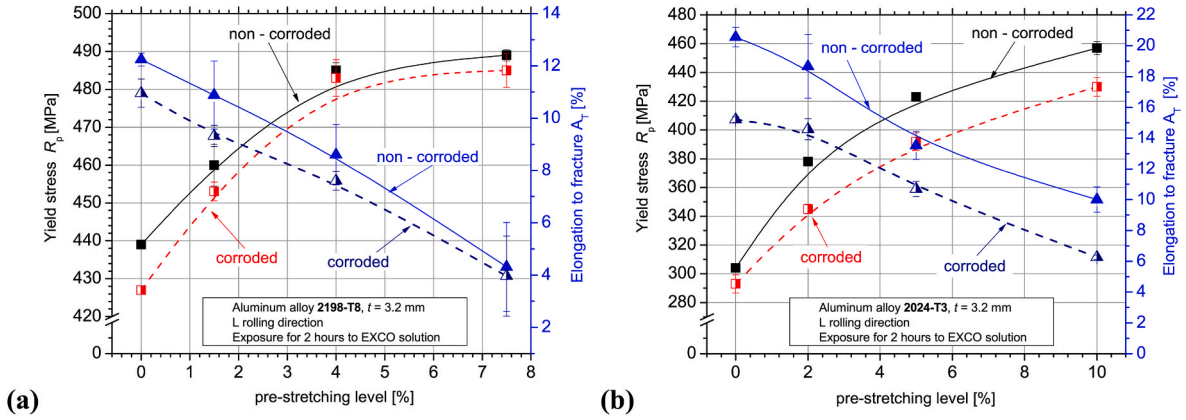

Fig. 13. The effect of pre-stretching and subsequent corrosion on yield stress R_p (left black Y-axis) and elongation to fracture A_T (right blue Y-axis) for (a) AA2198-T8 and (b) AA2024-T3.

degradation of the 2198-T8-1.5 %ps specimens were attributed to localised and intergranular corrosion; the latter of which results in the formation of corrosion-induced secondary cracking during subsequent tensile straining. As previously mentioned, IGC is more aggressive than crystallographic pitting [53], [83] and, therefore, these specimens reveal a larger degradation of A_T. With an increase in the level of pre-stretching (*i.e.*, more evenly distributed dislocation density and precipitation), a transition is observed towards intragranular corrosion, which is less detrimental to the A_T.

In general, the secondary cracking was observed concentrated within the necking area and along the specimen corners. Several secondary cracks were noticed in all the pre-stretched specimens (Fig. 15); however, in some cases secondary cracking was more intense and severe. SEM-EDS analysis revealed the presence of corrosion product within and surrounding the secondary cracks (refer to Fig. 16); supporting that they are likely a result of corrosion induced cracking (CIC).

In order to establish the degree of secondary cracking in the different pre-stretched samples to correlate it with the tensile properties results, *i.e.*, A_T decreased percentage, the cracks were counted as a function of distance from the fracture surface. Additionally, the widths of the cracks were also measured as depicted in Fig. 17.

From the above analysis, the results were extracted as shown in Fig. 17 plotting the secondary crack densities (crack width per interval divided by cumulative crack width over section length) for the different

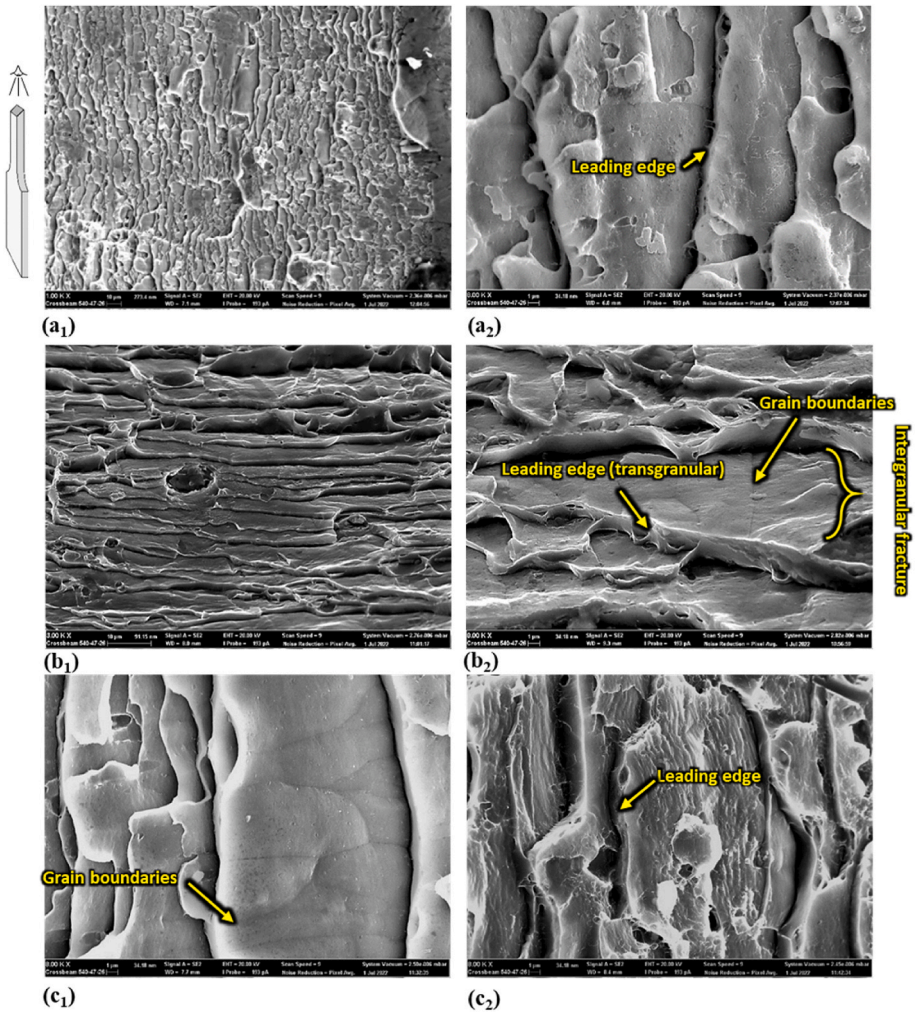

Fig. 14. Summary of the general fracture surface morphology observed throughout the conditions considered, using (a) the 2198-T8-2h_EXCO sample, (b) the 2198-T8-7.5 %ps-2h_EXCO sample and (c) the 2198-T8-7.5 %ps sample.

investigated pre-stretching levels of AA2198-T8 and correlate it with total elongation to fracture A_T (Fig. 17(a)) as well as charge transfer resistance R_{CT} (Fig. 17(b)). It is worth mentioning that the worst case of secondary cracking was taken into consideration. It is noticed that 2198-T8-1.5 %ps-2h_EXCO specimens revealed the highest secondary cracks density followed by 2198-T8-4.0 %ps-2h_EXCO and 2198-T8-7.5 %ps-2h_EXCO samples. Lower values for the crack densities indicates lower penetration depth (more superficial cracks) whilst at the same time incorporating the quantity of the cracks. The secondary cracks width tendency with increasing pre-stretching level is in accordance with A_T decrease percentage, whilst R_{CT} was found to be conversely analogous. Fig. 17(c) presents the SEM micrograph of 2198-T8-4 %ps-2h_EXCO specimen in order to illustrate the method used for the calculation of secondary crack widths.

Furthermore, the chart of Fig. 18 comparing the overall crack width densities as a function of distance from the fractured surface also shows that the sample 2198-T8-1.5 %ps-2h_EXCO stands out with most cracks on its surface, even at locations away from the fractured surface. This was not the case for 2198-T8-7.5 %ps-2h_EXCO specimens, in which several secondary cracks with high width were mostly observed near the fracture surface but little to no cracks further away. More and wider cracks in the intrinsic protective oxide layer provide more and easier channels for the 3.5 *wt* % NaCl solution to reach the alloy's surface and, therefore, result in corrosion intensification. These results are in accordance with the respective of total elongation A_T percentage decrease as well as with the respective of electrochemical measurements, where the sample with the lowest R_{CT} vs. corrosion exposure time curve, and the most negative E_{corr} potential, *i.e.*, most susceptible to corrosion attack, was found to be the 2198-T8-1.5 %ps.

4. Discussion

In order to explain the difference of the corrosion behaviour between the different pre-stretching levels of AA2198-T8, the results of microscopic and macroscopic analyses as well as mechanical testing were further examined and analysed.

The lower charge transfer resistance values of the 2198-T8-1.5 %ps specimens revealed by the EIS results (section 3.3) are reflected in the results of total elongation to fracture, presented in Fig. 19. In this figure, the A_T percentage decrease is plotted against the normalized pre-stretching level, that was defined as the level of pre-stretching as a fraction of the total elongation to fracture A_T. As can be seen from the figure and for the AA2198-T8 alloy, the 2198-T8-1.5 %ps specimens exhibited the highest degradation percentage of A_T due to corrosion, *i.e.*, approximately 14 %, followed by 2198-T8-4 %ps. Corrosion-induced degradation reduced to approximately 8 % (almost half of the respective percentage in 2198-T8-1.5 %ps) after 7.5 %ps level, reaching to lower decrease percentage even from the AA2198-T8 specimens.

In total, it is observed that the pre-stretching process deteriorates the material's corrosion behaviour for the first stages of stretching, *i.e.*, 2198-T8-1.5 %ps in the present case, while a reduction of the degradation effect is noticed with increasing pre-stretching level due to

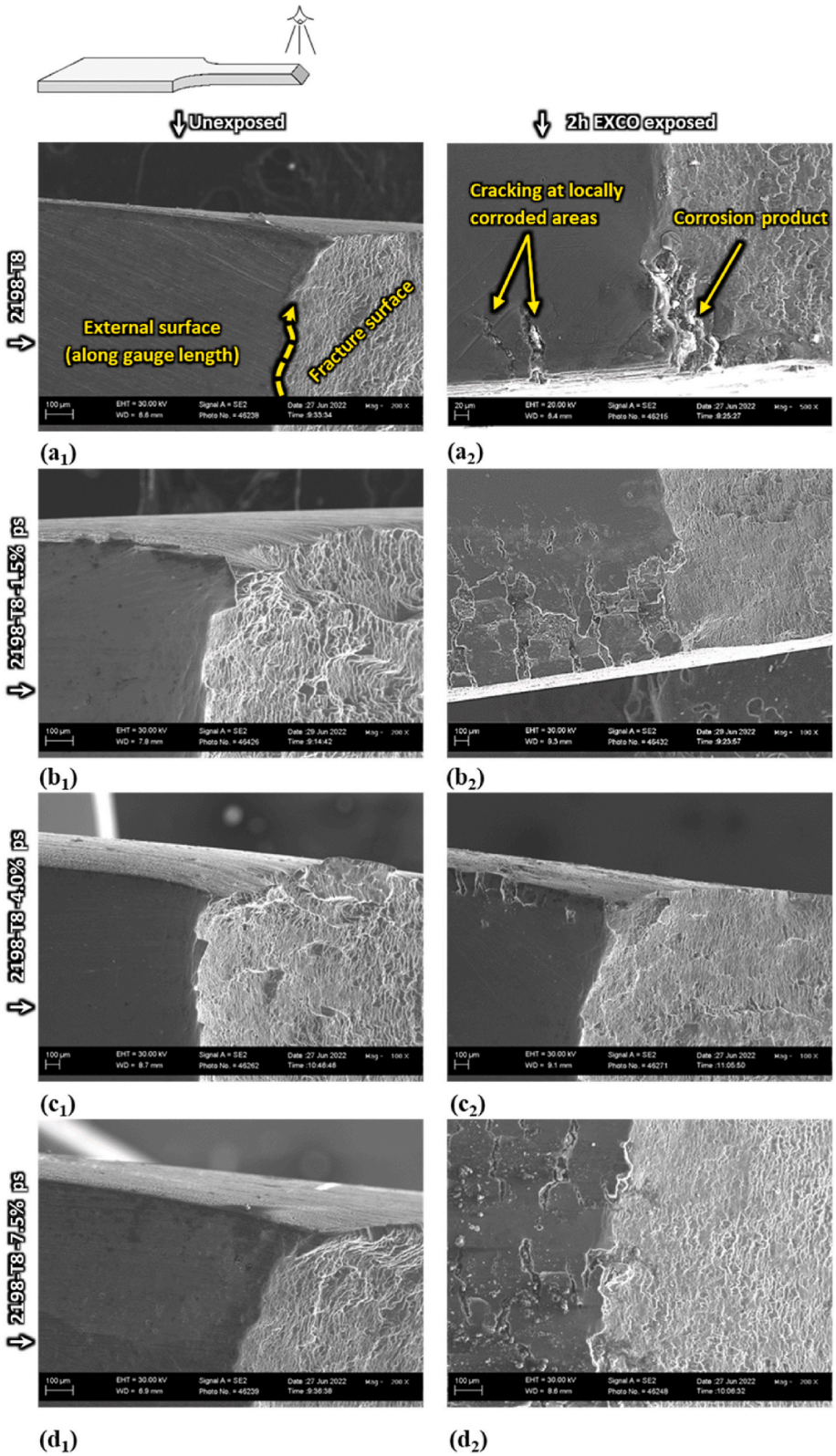

Fig. 15. SEM fractographs showing the effect of pre-stretching and EXCO exposure on the surface damage behaviour of AA2198, by comparing the unexposed specimens (noted as subscript 1) to the exposed specimens (noted as subscript 2); (a) AA2198-T8, (b) AA2198-T8-1.5 %ps, (c) AA2198-T8-4.0 %ps and (d) AA2198-T8-7.5 %ps.

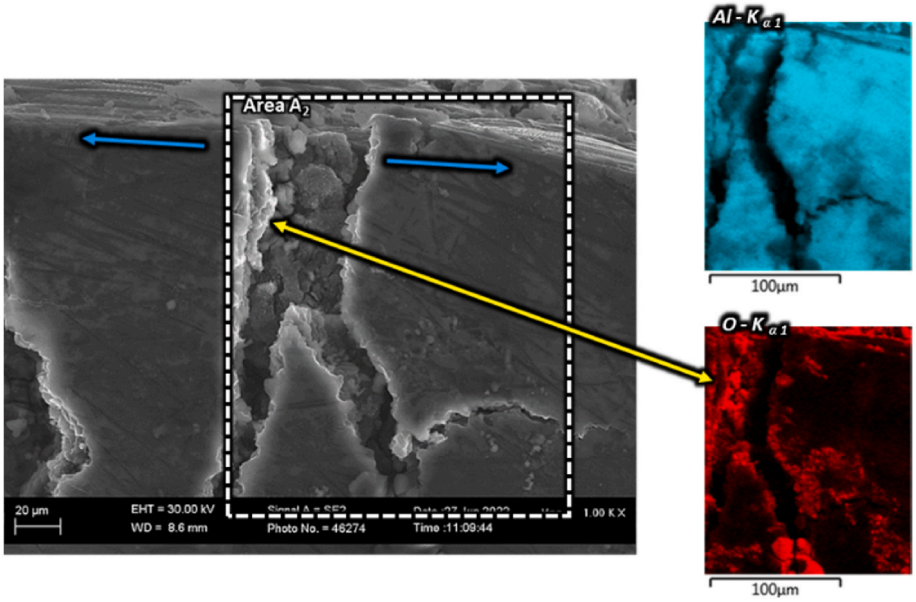

Fig. 16. (a) SEM image of secondary cracking and SEM-EDS analysis (of the area depicted by A_2) of the corrosion induced cracks observed near the specimen corner of 2198-T8-4.0 %ps-2h_EXCO specimen, following tensile fracture and indicating the presence of a highly oxidized product within the cracks (the blue arrows indicate the loading direction).

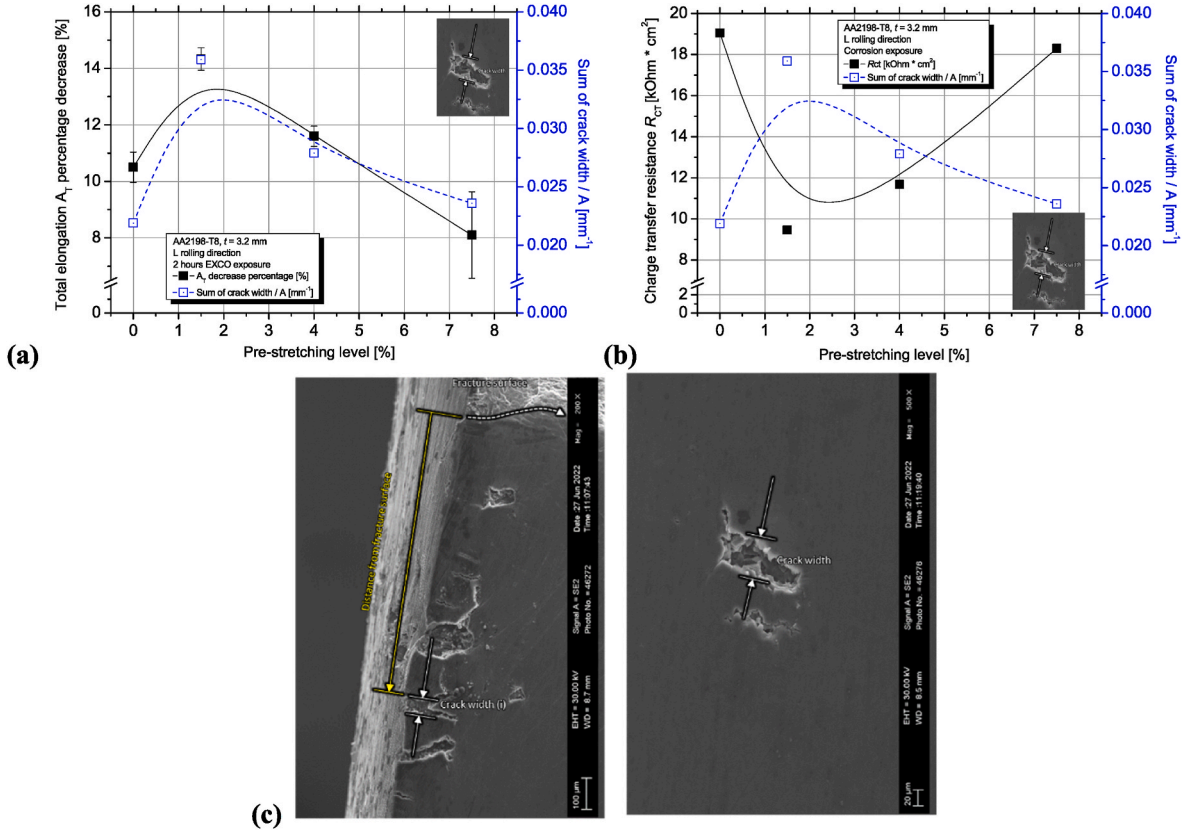

Fig. 17. Correlation of total elongation to fracture (a) and charge transfer resistance (b) with secondary cracking (right Y-axis) for the different pre-stretching levels of AA2198-T8 and (c) measuring details of cracking length.

recovery of the grain structure, with more HAGBs, at higher levels of pre-strain. Nonetheless, despite the reduced corrosion resistance degradation observed with increasing pre-stretching level, the corrosion was found to propagate easier and in higher rates for higher pre-stretching levels (*i.e.*, i_{corr} values and slope of R_{CT} vs. time curves). This phenomenon is attributed to the different corrosion attack mechanism for the different pre-stretching levels; for instance, the 2198-T8-1.5 %ps samples were found to exhibit intergranular corrosion attack with severe secondary cracking on the fractured surface. As can be noticed from the trend in Fig. 17(a), the secondary cracking seems to

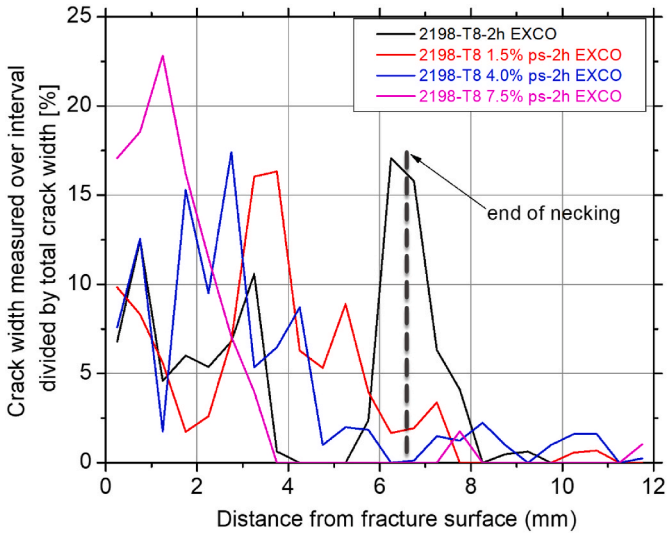

Fig. 18. Line-graph showing the overall crack-width densities as a function of distance from the fracture surface for AA2198-T8 at different pre-stretching levels.

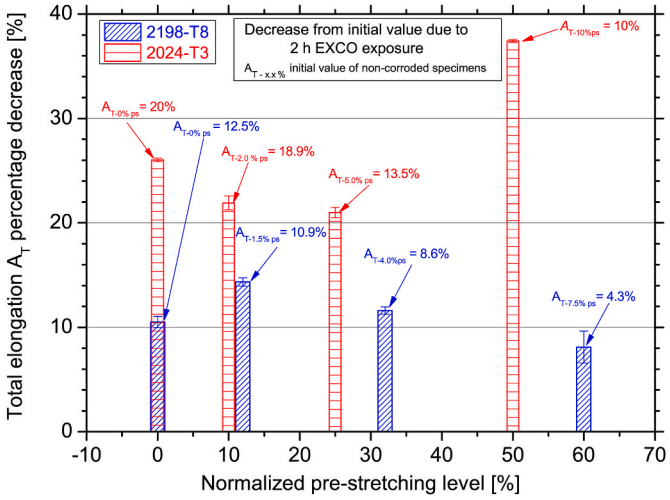

Fig. 19. Corrosion-induced degradation percentage of elongation to fracture A_T for the various pre-stretching levels of AA2198-T8 and AA2024-T3.

highly contribute to the A_T degradation as well as R_{CT}. Secondary cracking forms due to grain boundary embrittlement and segregation, as was also mentioned in [83], [86], and this is the reason why specimens pre-stretched at 1.5 % level exhibited the highest corrosion-induced degradation of elongation to fracture. Ma *et* al. [31] and Huang *et* al. [48] conducting similar work on other Al–Cu–Li alloys, found similar results, where high density of deformation or stored energy in grains were associated with high levels of corrosion. In the present work it was shown that highly deformed grains present in the 1.5 % pre-stretched sample, Figs. 5 and 6(c), have high thermodynamic activity, thus leading to the IGC and increased secondary cracking observed in Fig. 17(a). There is a direct correlation in terms of the charge transfer resistance, grain stored energy from pre-stretching and the decrease in total elongation following corrosion exposure.

The difference observed in the mechanism of attack is believed to be linked to deformation-induced chemical heterogeneity. The T8 temper designation refers to the artificially under-aged condition of the alloy. According to the literature [87] the elevated temperature treatment (artificial ageing) allows for the nucleation and growth of the T_1 (Al_2CuLi) phase in this alloy, with the nucleation promoted/assisted by dislocations (*i.e.*, favoured by cold work). However, due to the alloy being in the under-aged condition in the present study, slight matrix supersaturation may still be present with regards to the principal alloying elements. Nonetheless, since the pre-stretching was performed at ambient temperatures and sometime before the tensile test, nucleation of the T_1 phase is not possible since this phase requires elevated temperatures to nucleate. According to the work by Zhang et al. [87], the δ'-phase may nucleate at ambient temperatures during natural ageing, with the nucleation also promoted/assisted by dislocations (similar to the findings by Cassada et al. [88]). As was already discussed in section 3.4 (Fig. 12) regarding the increased yield stress and the extended "easy-glide" region which was observed at low strain levels (*i.e.*, 1.5 %), dislocation pinning via dislocation-assisted δ'-phase nucleation is probable, with the under-aged material condition providing the driving force (supersaturated matrix) for the nucleation, whilst the presence of dislocations facilitate the nucleation of the phase.

Furthermore, heterogeneous deformation of neighbouring grains was revealed by EBSD analysis (section 3.2). Therefore, during the pre-stretching operation, certain grains would have a more favourable orientation to the deformation axis and, consequently, will deform with relatively higher ease. This, in turn, implies that higher dislocation densities will be associated with these more-favourably orientated grains and, as such, a higher degree of dislocation-assisted δ'-phase nucleation may be expected within these grains. Evidence for this may also be seen in Fig. 5. Although more uniformly distributed than the other pre-stretching conditions, the deformation observed within the purely pre-stretched AA2198-T8-1.5 %ps material condition varies from grain to grain.

Combining the above-mentioned considerations and observations, it is proposed that the resulting heterogeneous deformation within neighbouring grains may allow for variations in the volume fraction of δ'-phase nucleation between them. Therefore, chemical heterogeneity is induced between these grains, resulting from unequal removal of *Li* in solid solution. The resulting micro-galvanic coupling allows for corrosion attack that follows along the periphery of the more anodic grain (in accordance with the work by Zhang et al. [51]), translating into IGC attack. The proposed method may also explain the increased susceptibility to attack (lower R_{CT}) for the 1.5 % pre-stretched condition, accompanied by a reduced corrosion rate (lower i_{corr}). That is, although corrosion may initiate at numerous sites (due increased volume fraction of grain boundaries and consequently δ'-phase nucleation), the attack is localised along the grain boundaries of the material (reduced i_{corr}). This is shown schematically in Fig. 20(a).

At pre-stretching levels of 4 % and higher, the EBSD results indicated that recovery is favoured. From Fig. 5, it can be observed that sub-grain boundaries (SGBs) have started to form after 4 % pre-stretching level, with the SGBs becoming more defined after 7.5 % pre-stretching level. According to the misorientation maps (Fig. 5), certain grains will have high densities of these sub-grain boundaries, whilst other grains are seemingly unaffected, revealing that deformation is concentrated to specific grains in these stretching levels. According to the proposed mechanism for the 2198-T8-1.5 %ps specimens, δ'-phase nucleation is expected to be higher within the more deformed grains. Therefore, more *Li* is removed from the matrix of the more deformed grains, where the sub-grain boundaries may also serve as the preferred sites for δ'-phase nucleation and, as such, a transition is seen towards crystallographic/transgranular attack. According to this proposed mechanism, the sites available for the initiation of corrosion is reduced, increasing R_{CT}. However, due to a larger difference in the deformation (and δ'-phase nucleation) observed in neighbouring grains, the rate of attack (i_{corr}) is increased (larger potential difference). With the preferred nucleation of the δ'-phase within SGBs, corrosion may rather be initiated by dissolution of the anodic δ' phase – formed within the SGBs – followed by crystallographic pitting attack of the more anodic matrix (refer to Fig. 20 (b)). Nevertheless, a mixed-mode corrosion attack moving towards transgranular corrosion mechanism was found to dominate in higher

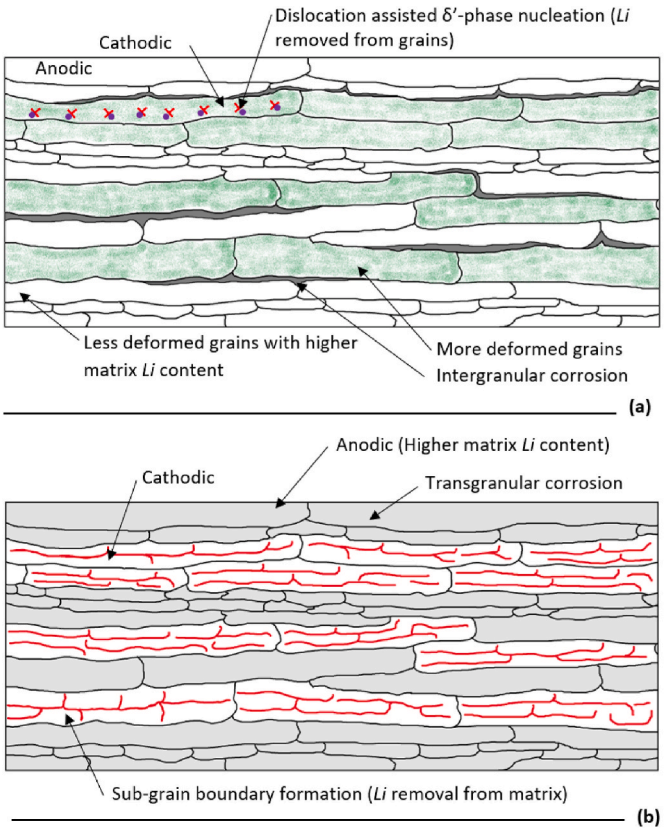

Fig. 20. Schematic diagrams illustrating the corrosion mechanism for (a) AA2198-T8-1.5 %ps-2h_EXCO and (b) the higher prestretching levels (AA2198-T8-4 %ps-2h_EXCO and AA2198-T8-7.ps-2h_EXCO).

pre-stretched samples due to recovery and the formation of sub-grain boundaries, due to a reduced dependency of the corrosion mechanism on the presence of LAGBs.

5. Summary and conclusions

In the present work, the effect of the magnitude of the pre-stretching process on the corrosion attack mechanism of AA2198-T8 specimens is assessed. The findings of the work can be summarized as follows.

1) Pre-stretching at low levels was found to be detrimental for corrosion initiation and corrosion-induced degradation of tensile mechanical properties, and especially for elongation to fracture (ductility). Approximately 14 % decrease of A_T due to corrosion exposure was observed for the AA2198-T8-1.5 %ps specimens, while the respective decrease for AA2198-T8-7.5 %ps specimens was diminished to 8 %. Additionally, the charge transfer resistance of the specimens pre-stretched at 1.5 % pre-deformation level was found to be the lowest, while an improvement was noticed with further pre-stretching. Similarly, the cumulative crack widths of secondary cracks present on the gauge length surface was found to be at a maximum for the AA2198-T8-1.5 %ps specimens. These differences are attributed to the different corrosion attack mechanisms active at the individual levels of pre-stretching investigated, owing to the different grain structures and substructures and its impact on the corrosion initiation resistance of the material.
2) Intergranular corrosion attack was found to be the dominant degradation mechanism for the specimens characterized by low-angle grain morphology (i.e., AA2198-T8-1.5 %ps), triggered by the high density of grain boundaries and associated dislocation density. On the contrary, a transition to transgranular corrosion attack was observed for the specimens in higher pre-stretching levels due to the recovery of the grain structure and the reduction of grain boundaries density.
3) Despite of the detrimental effect of low-level pre-stretching on corrosion initiation and corrosion-induced tensile properties degradation, the propagation rate of corrosion appeared to be almost the same for all samples, based on their similar i_{corr} values. However, only the Tafel plots of pre-stretched samples had an additional corrosion peak that appeared at 0.1 V more anodic of E_{corr}, which can be ascribed to pre-stretching-induced onset of a parallelly occurring localised corrosion inside the formed cracks.
4) The AA2198-T8 alloy showed superior resistance to corrosion-induced tensile property degradation at all levels of pre-stretching, compared to earlier generations of high-strength Al alloys such as AA2024-T3. The AA2198-T8 however did suffer from corrosion-induced tensile mechanical property degradation, with the 1.5 % ps level showing the greatest extent of degradation due to grain boundary embrittlement (secondary cracking), while increasing pre-stretching levels reduced the effect of corrosion attack, especially on the elongation to fracture A_T degradation. In contrast, the AA2024-T3 alloy is not essentially influenced by pre-stretching regarding the extent of corrosion degradation of the tensile properties.
5) Pre-stretching at higher levels enhances dynamic recovery and a higher concentration of dislocations inside grains, thus eliminating precipitate free zones (PFZs) and localised corrosion. Accordingly, higher levels of pre-stretching will lead to transgranular corrosion attack as opposed to the more aggressive intergranular corrosion observed at lower pre-stretching levels.

CRediT authorship contribution statement

Christina Margarita Charalampidou: Investigation, Experimental work, Data curation, Writing – original draft. **Christiaan C.E. Pretorius:** Investigation, Experimental work, Data curation, Writing – original draft. **Muhammed Salojee:** Experimental work, Data curation, Writing – original draft. **Dionysios Karousos:** Experimental work, Data curation. **Malika Khodja:** Investigation, Writing – review & editing. **Roelf J. Mostert:** Conceptualization, Methodology, Writing – review & editing. **Nikolaos D. Alexopoulos:** Conceptualization, Methodology, Writing – review & editing.

Declaration of competing interest

The authors declare that they have no known competing financial interests or personal relationships that could have appeared to influence the work reported in this paper.

Acknowledgements

This research work was financed by the Hellenic Foundation for Research and Innovation (H.F.R.I.) Greece, under the 2nd Call for H.F.R.I. Research Projects to support Faculty Members and Researchers (Proposal ID: 03385, MIS Acronym: CorLi, Title: Corrosion susceptibility, degradation and protection of advanced Al–Li aluminium alloys).

References

[1] Dursun T, Soutis C. Recent developments in advanced aircraft aluminium alloys. Mater Des 2014;56:862–71.
[2] European Commission. Directorate-General for Mobility and Transport, Directorate-General for Research and Innovation, Flightpath 2050 – europe's vision for aviation – maintaining global leadership and serving society's needs. Publications Office; 2011.
[3] Das S. Recycling and life cycle issues for lightweight vehicles. In: Mallick PK, editor. Materials, design and manufacturing for lightweight vehicles. Woodhead publishing series in composites science and engineering. Woodhead Publishing; 2010. p. 309–31.

[4] Rioja RJ, Liu J. The evolution of Al-Li base products for aerospace and space applications. Metall Mater Trans A 2012;43:3325–37.
[5] Boţilă LN. Considerations regarding aluminum alloys used in the aeronautic/aerospace industry and use of wire arc additive manufacturing WAAM for their industrial applications. Welding & Material Testing 2020;4:1–16.
[6] Srivatsan TS, Lavernia EJ, Prasad NE, Kutumbarao VV. Quasi-static strength, deformation, and fracture behavior of aluminum-lithium alloys. In: Eswara Prasad N, Gokhale Amol A, Wanhill RJH, editors. Aluminum – lithium alloys processing, properties and applications. USA: Butterworth-Heinemann; 2013.
[7] Alexopoulos ND, Migklis E, Stylianos A, Myriounis DP. Fatigue behavior of the aeronautical Al–Li (2198) aluminum alloy under constant amplitude loading. Int. J. Fatigue 2013;56:95–105.
[8] Alexopoulos ND, Proiou A, Dietzel W, Blawert C, Heitmann V, Zheludkevich M, Kourkoulis SK. Mechanical properties degradation of (Al-Cu-Li) 2198 alloy due to corrosion exposure. Procedia Struct. Integ. 2016;2:597–603.
[9] Moreto JA, Broday EE, Rossino LS, Fernandes JCS, Bose Filho WW. Effect of localized corrosion on fatigue–crack growth in 2524-T3 and 2198-t851 aluminum alloys used as aircraft materials. J Mater Eng Perform 2018;27:1917–26.
[10] Zou Y, Chen X, Chen B. Corrosion behavior of 2198 Al–Cu–Li alloy in different aging stages in 3.5 wt % NaCl aqueous solution. J Mater Res 2018:1–12.
[11] Moreto JA, Gamboni O, Ruchert COFT, Romagnoli F, Moreira MF, Beneduce F, Bose Filho WW. Corrosion and fatigue behavior of new Al alloys. Procedia Eng 2011;10:1521–6.
[12] Moreto JA, Marino CEB, Bose Filho WW, Rocha LA, Fernandes JCS. SVET, SKP and EIS study of the corrosion behaviour of high strength Al and Al–Li alloys used in aircraft fabrication. Corros Sci 2014;84:30–41.
[13] Milagre MX, Donatus U, Machado CSC, Araujo JV, da Silva RMP, de Viveiros BVG, Astarita A, Costa I. Comparison of the corrosion resistance of an Al–Cu alloy and an Al–Cu–Li alloy. Corros. Eng. Sci. Technol. 2019;54:402–12.
[14] Araujo JV de S, Milagre MX, Ferreira RO, Machado C de SC, Bugarin A de FS, Machado IF, Costa I. Exfoliation and intergranular corrosion resistance of the 2198 Al–Cu–Li alloy with different thermomechanical treatments. Corros. Mater. 2020:1–14.
[15] Li H, Tanga Y, Zeng Z, Zheng Z, Zheng F. Effect of ageing time on strength and microstructures of an Al–Cu–Li–Zn–Mg–Mn–Zr alloy. Mater. Sci. Eng. A 2008;498:314–20.
[16] Prasad NE, Gokhale AA, Wanhill RJH. In: Aluminum-Lithium alloys processing, properties and applications. first ed. USA: Butterworth-Heinemann; 2013.
[17] Dorin T, De Geuser F, Lefebvre W, Sigli C, Deschamps A. Strengthening mechanisms of T1 precipitates and their influence on the plasticity of an Al–Cu–Li alloy. Materials Science & Engineering A 2014;605:119–26.
[18] Blankenship CP, Starke EA. Improved toughness in Al–Li–Cu–Mg–Ag–Zr alloy X2095. Scripta Metall Mater 1992;26:1719–22.
[19] Blankenship CP, Starke EA. Mechanical behavior of double-aged AA8090. Metall Mater Trans A 1993;24:833–41.
[20] Tosten MH, Vasudevan AK, Howell PR. Microstructural development in Al_2 % Li_3 %Cu alloy. In: Baker C, Gregson PJ, Harris SJ, Peel CJ, editors. Proceedings of the third international conference on Aluminium_Lithium alloys. London: The Institute of Metals; 1986. p. 483–9.
[21] Nie JF, Muddle BC, Polmear IJ. The effect of precipitate shape and orientation on dispersion strengthening in high strength aluminium alloys. Mater Sci Forum 1996:1257–62.
[22] Abd El-Aty A, Xu Y, Guo X, Zhang S-H, Ma Y, Chen D. Strengthening mechanisms, deformation behavior, and anisotropic mechanical properties of Al-Li alloys: a review. J Adv Res 2018;10:49–67.
[23] Itoh G, Cui Q, Kanno M. Effects of a small addition of magnesium and silver on the precipitation of T1 phase in an A1-4 %Cu-l.l %Li-0.2 % Zr alloy. Mater. Sci. Eng. A 1996;211:128–37.
[24] Araullo-Peters V, Gault B, Geuser F, Deschamps A, Cairney JM. Microstructural evolution during ageing of Al–Cu–Li–x alloys. Acta Mater 2014;66:199–208.
[25] Howe JM, Lee J, Vasudévan AK. Structure and deformation behavior of T1 precipitate plates in an Al- 2Li- 1 Cu alloy. Metall Trans A 1988;19:2911–20.
[26] Nie JF, Muddle BC. On the form of the age-hardening response in high strength aluminium alloys. Mater. Sci. Eng. A 2001;319–321:448–51.
[27] Boag A, Hughes AE, Glenn AM, Muster TH, McCulloch D. Corrosion of AA2024-T3 Part I: localised corrosion of isolated IM particles. Corros Sci 2011;53:17–26.
[28] Guillaumin V, Mankowski G. Localized corrosion of 2024-T351 aluminum alloy in chloride media. Corros Sci 1999;41:421–38.
[29] Blanc C, Lavelle B, Mankowski G. The role of precipitates enriched with copper on the susceptibility to pitting corrosion of the 2024 aluminum alloy. Corros Sci 1997;39:495–510.
[30] Ma Y, Zhou X, Liao Y, Yi Y, Wu H, Wang Z, Huang W. Localised corrosion in AA2099-T83 aluminium-lithium alloy: the role of grain orientation. Corros Sci 2015;107:41–8.
[31] Ma Y, Zhou X, Huang W, Liao Y, Chen X, Zhang X, Thompson GE. Crystallographic defects induced localised corrosion in AA2099-T8 aluminium alloy. Corros. Eng. Sci. Technol. 2015;50:420–4.
[32] Huang BP, Zheng ZQ. Effects of Li content on precipitation in Al–Cu–(Li)–Mg–Ag–Zr alloys. Scr Mater 1998;38:357–62.
[33] Decreus B, Deschamps A, De Geuser F, Donnadieu P, Sigli C, Weyland M. The influence of Cu/Li ratio on precipitation in Al–Cu–Li–x alloys. Acta Material 2013;61:2207–18.
[34] Kim JH, Jeun JH, Chun HJ, Lee YR, Yoo JT, Yoon JH, Lee HS. Effect of precipitates on mechanical properties of AA2195. J Alloys Compd 2016;669:187–98.
[35] Proton V, Alexis J, Andrieu E, Delfosse J, Deschamps A, De Geuser F, Lafont MC, Blanc C. The influence of artificial ageing on the corrosion behaviour of a 2050 aluminium-copper-lithium alloy. Corros Sci 2014;80:494–502.
[36] Machado C de SC, da Silva RMP, Araujo JV de S, Milagre MXr, Donatus U, de Viveiros BVG, Klumpp RE, Costa I. Influence of chloride ions concentration on the development of severe localised corrosion and its effects on the electrochemical response of the 2198-T8 alloy. Corros. Eng. Sci. Technol. 2021;56:341–50.
[37] Araujo JV de S, da Silva RMP, Donatus U, Machado C de SC, Costa I. Microstructural, electrochemical and localized corrosion characterization of the aa2198-t851 alloy. Mater Res 2020;23.
[38] Wanhill RJH. Aerospace applications of aluminum–lithium alloys. In: Eswara Prasad N, Gokhale Amol A, Wanhill RJH, editors. Aluminum-lithium alloys. Butterworth-Heinemann; 2014. p. 503–35.
[39] Maeno T, Mori K, Yachi R. Hot stamping of high-strength aluminium alloy aircraft parts using quick heating. CIRP Annals 2017;66:269–72.
[40] Martin JW. Precipitation hardening. second ed. Oxford: Butterworth-Heinemann; 1998.
[41] Gable BM, Zhu AW, Csontos AA, Starke Jr EA. The role of plastic deformation on the competitive microstructural evolution and mechanical properties of a novel Al-Li-Cu-X alloy. J. Light Metals 2001;1:1–14.
[42] Cassada WA, Shiflet GJ, Starke EA. The effect of plastic deformation on Al2CuLi (T1) precipitation. Metall Trans A 1991;22:299–306.
[43] Ringer SP, Muddle BC, Polmear IJ. Effects of cold work on precipitation in Al-Cu-Mg-(Ag) and Al-Cu-Li-(Mg-Ag) alloys. Metall Mater Trans A 1995;26:1659–71.
[44] Lu YL, Wang J, Li X, Chen Y, Zhou D, Zhou G, Xu W. Effect of pre-deformation on the microstructures and properties of 2219 aluminum alloy during aging treatment. J Alloys Compd 2017;699:1140–5.
[45] Kang YH, Wang XX, Zhang N, Yan H, Chen RS. Effect of pre-deformation on microstructure and mechanical properties of WE43 magnesium alloy. Mater. Sci. Eng. A 2017;689:435–45.
[46] Wang HM, Yi YP, Huang SQ. Influence of pre-deformation and subsequent ageing on the hardening behavior and microstructure of 2219 aluminum alloy forgings. J Alloys Compd 2016;685:941–8.
[47] Rodgers BI, Prangnell PB. Quantification of the influence of increased pre-stretching on microstructure-strength relationships in the Al-Cu-Li alloy AA2195. Acta Mater 2016;108:55–67.
[48] Huang W, Ma Y, Zhou X, Meng X, Liao Y, Chai L, Yi Y, Zhang X. Correlation between localized plastic deformation and localized corrosion in AA2099 aluminum-lithium alloy. Surf Interface Anal 2015;48:838–42.
[49] Ma Y, Zhou X, Huang W, Liao Y, Chen X, Zhang X, Thompson GE. Crystallographic defects induced localised corrosion in AA2099-T8 aluminium alloy. Corrosion Eng Sci Technol 2015;50:420–4.
[50] Zhang X, Zhou X, Cai G, Yu Y, Lu X, Jiao Y, Dong Z. The influence of stored energy on grain boundary chemistry and intergranular corrosion development in AA2024-T3 alloy. Materials 2018;11:2299.
[51] Zang X, Jiao Y, Yu Y, Liu B, Hashimoto T, Liu H, Dong Z. Intergranular corrosion in AA2024-T3 aluminium alloy: the influence of stored energy and prediction. Corros Sci 2019;155:1–12.
[52] Zhang Y, Ling J, Li H-G, Luo X-Y, Ba Z-X. Effect of pre-deformation and artificial aging on fatigue life of 2198 Al-Li alloy. Mater Res Express 2020;7:046509.
[53] Wang Y, Ma X, Xi H, Zhao G, Xu X, Chen X. Effects of pre-stretching and aging treatments on microstructure, mechanical properties, and corrosion behavior of spray-formed Al-Li alloy 2195. JMEPEG 2020;29:6960–73.
[54] ASTM B918, Aluminium alloy nomenclature and temper designations.
[55] Charalampidou C-M, Tazlakidou F, Zheludkevich M, Kourkoulis S, Alexopoulos ND. The effect of solution aggressiveness on the corrosion-induced degradation mechanism of Al-Cu-Li 2198 alloy. Theor Appl Fract Mech 2024;129:10424.
[56] ASTM E8M. Standard test methods for tension testing of metallic materials. West Conshohocken, PA: ASTM International; 2009.
[57] ASTM G1. Standard practice for preparing, cleaning, and evaluating corrosion test specimens. West Conshohocken, PA: ASTM International; 1999.
[58] ASTM G34. Standard test method for exfoliation corrosion susceptibility in 2XXX and 7XXX series aluminum alloys (EXCO test). West Conshohocken, PA: ASTM International; 2001.
[59] Sprowls DO, Walsh JD, Shumaker MB. Simplified exfoliation testing of aluminum alloys, vol. 516. ASTM STP; 1972. https://doi.org/10.1520/STP35415S.
[60] Alexopoulos ND, Proiou A, Dietzel W, Blawert C, Heitmann V, Zheludkevich M, Kourkoulis SK. Mechanical properties degradation of (Al-Cu-Li) 2198 alloy due to corrosion exposure. Procedia Struct Integr 2016;2:597–603.
[61] Charalampidou CM, Tazlakidou F, Kourkoulis SK, Alexopoulos ND. The effect of solution aggressiveness on corrosion-induced mechanical properties degradation of aeronautical aluminum alloy 2198. Procedia Struct Integr 2022;42:1708–13.
[62] Alexopoulos ND, Velonaki Z, Stergiou CI, Kourkoulis SK. The effect of artificial ageing heat treatments on the corrosion-induced hydrogen embrittlement of 2024 (Al–Cu) aluminium alloy. Corros Sci 2016;102:413–24.
[63] Covino Jr BS. Introduction to corrosion testing and evaluation, corrosion: fundamentals, testing, and protection, 13A. ASM International; 2003. p. 419. ASM Handbook.
[64] Guérin M, Andrieu E, Odemer G, Alexis J, Blanc C. Effect of varying conditions of exposure to an aggressive medium on the corrosion behavior of the 2050 Al–Cu–Li alloy. Corros Sci 2014;85:455–70.
[65] Engler O, Randle V. Texture analysis: macrotexture, microtexture and orientation mapping. second ed. London: CRC Press; 2010.

[66] Prasad NE, Gokhale A, Wanhill aRJ H. Chapter 5: texture and its effects on properties in aluminum À lithium alloys. In: Aluminum-Lithium alloys : processing, properties, and applications. Elsevier Science & Technology; 2013. p. 139–64.
[67] Hirsch J, Lumley R, editors. Fundamentals of aluminum metallurgy: production, processing and applications. Cambridge: Woodhead Publishing; 2010.
[68] He G, Tan L, Liu F, Huang L, Jiang ZH. Strain amount dependent grain size and orientation developments during hot compression of a polycrystalline nickel based superalloy. Materials 2017;10:1–14.
[69] Pirgazi LA. Texture formation in metal alloys with cubic crystal structures. Mater Sci Technol 2016;32:1303–15.
[70] de Sousa Araujo JV, de Fatima Santos Bugarin A, Donatus U, de Souza Carvalho Machado C, Queiroz FM, Terada M, Astarita A, Costa I. Thermomechanical treatment and corrosion resistance correlation in the AA2198 Al-Cu-Li alloy. Corros. Eng., Sci. Technol. 2019;1:575–86.
[71] Holroyd NJH, Scamans GM, Newman RC, Vasudevan AK, Heinemann Butterworth-, editors. Corrosion and stress corrosion of aluminum–lithium alloys in aluminum-lithium alloys processing. Properties, and Applications; 2014. p. 457–500.
[72] Huang K, Loge RE. A review of dynamic recrystallization phenomena in metallic materials. Mater Des 2016;111:548–74.
[73] Raabe D. Recovery and recrystallisation: phenomenon, physics, models, simulations. In: Laughlin David E, Hono Kazuhiro, editors. Physical metallurgy; 2014. p. 2291–396.
[74] Rakshit R, Bairagi D, Panda SK, Mandal S. Influence of strain path dependent microstructural evolution on corrosion behaviour in Al-Li alloy. Mater Lett 2023; 348:1–7.
[75] Zhang C, Liu M, Meng Z, Zhang Q, Zhao G, Chen L, Zhang H, Wang J. Microstructure evolution and precipitation characteristics of spray-formed and subsequently extruded 2195 Al-Li alloy plate during solution and aging process. J. Mater. Process. Tech. 2020;283:116718.
[76] Lasia A. Dispersion of impedances at solid electrodes. In: Electrochemical impedance spectroscopy and its applications. New York: Springer; 2014.
[77] Schmutz P, Frankel GS. Characterization of AA2024-T3 by scanning kelvin probe force microscopy. J Electrochem Soc 2006;145:2285–95.
[78] Prakashaiah BG, Kumara DV, Pandith AA, Shetty AN, Amitha Rani BE. Corrosion inhibition of 2024-T3 aluminum alloy in 3.5 % NaCl by thiosemicarbazone derivatives. Corros Sci 2018;136:326–38.
[79] Lamaka SV, Zheludkevich ML, Yasakau KA, Montemor MF, Ferreira MGS. High effective organic corrosion inhibitors for 2024 aluminum alloy. Electrochim Acta 2007;52:7231–47.
[80] Makuch N. The importance of phase composition for corrosion resistance of borided layers produced on nickel alloys. Materials 2020;13:5131.
[81] Jinlong L, Tongxiang L, Chen W, Ting G. The passive film characteristics of several plastic deformation 2099 Al-Li alloy. J Alloys Compd 2016;662:143–9.
[82] Zhang X, Zhou S, Zhang H, Liu X, Yang H. Lüders strain of the fine-grained material under the electric current. Mater Sci Eng 2021;825:141924.
[83] Charalampidou CM, Pretorius CE, Mostert RJ, Alexopoulos ND. Effect of solution aggressiveness on the crack growth resistance and cracking mechanism of AA2024-T3. Corros 2021;77:1029–40.
[84] Guo G, Li Y, Li H, Peng X, Li J, Xu G. Quantitative effects of pre-deformation prior to non-isothermal aging on the mechanical properties-microstructure relationships in an Al-3.5Cu-1.01Li alloy. Mater Des 2022;223:1–14.
[85] Kolman DG. Liquid metal induced embrittlement in corrosion: fundamentals, testing, and protection. In: ASM handbook, 13A. ASM International; 2003. p. 381–92.
[86] Jones RH. Stress-corrosion cracking in corrosion: fundamentals, testing, and protection. In: ASM handbook, 13A. ASM International; 2003. p. 346–66.
[87] Zang S, Zeng W, Yang W, Shi C, Wang H. Ageing response of Al-Cu-Li 2198 alloy. Mater Des 2014;63:368–74.
[88] Cassada WA, Shiflet GJ, Jesser Wa. Heterogeneous nucleation and growth of δ' in Al-8 at % Li. Acta Metall Mater 1992;40:2101–11.